

An Apparatus for the Study of Corrosion and Tribocorrosion of Metals Induced by the Flow of Highly Turbulent Aqueous Solutions

R. W. Hendricks, P. K. Todoroff, R. C. Taylor, W. G. Wenger and E. A. Cothron
Materials Science and Engineering Department, Virginia Polytechnic Institute and State University, Blacksburg, VA 24061, USA,

robert.hendricks@vt.edu

Abstract

An apparatus to study tribocorrosion of materials in both laminar and highly turbulent flow of aqueous solutions under reliably and accurately controlled environmental conditions for long durations is reported. The apparatus simulates single direction, circulating turbulent fluid flow, as opposed to common laboratory “bath” style configurations through the use of a custom-built corrosion resistant loop that comprises 11 m of DN 50 CPVC piping through which aqueous solutions are pumped via either a primary 3.7 kW centrifugal impeller pump or a secondary 54 W diaphragm pump. There is a 3.5 kW resistance heating element and a heat exchanger to provide a wide operating range of conditions to conduct environmental simulations to test both material performance, growth of passivation layers, and mechanisms of degradation. Flow rates ranging from 0–10 L/s and temperatures from 11 °C to 80 °C may be readily investigated. These flow rates correspond to Reynolds numbers from 200 to 300,000 at room temperature (900,000 at the maximum operating temperature of 80 °C). Environmental, hydrodynamic, and material performance properties are measured through a wide variety of in-situ sensors that are monitored and recorded via a data acquisition routine written as part of the apparatus monitoring system. Instrumentation includes three digital pressure gages for monitoring the line pressure at critical locations, a turbine flow sensor for monitoring the flow rate, as well as a dissolved oxygen sensor, two pH sensors, two conductivity sensors, and several thermocouples mounted at various locations to monitor solution chemistry. Two identical experimental bays allow for a wide variety of testing sections including a custom-designed universal sample chamber to study inserted orifice plates simulating valves and flow conditioners, commercial corrosion probes interfaced with commercial pipe components, or custom sensors to study the wall shear to remove protective coatings. The apparatus approaches tribocorrosion from an interdisciplinary approach by using computational simulations and

measured conditions of hydrodynamics and electrochemistry to perform a comprehensive study with in-depth characterization of the environment. Performance of the apparatus is shown through an expansive study of its fluid dynamics behaviour including calibration of the relationship between the pump motor frequency and the volumetric flow rate and the effect of pressure thereon, the effect of pumping speed on the temperature of the fluid and the characteristics of the heat exchanger required for its control, the loss factors of the various components of the loop, and the flow factors of various experiments and the relationship between the loss and flow factors.

Keywords: corrosion, corrosion loop, erosion, erosion-corrosion, tribocorrosion, flow accelerated corrosion, flow-related materials degradation, high turbulence flow, corrosion instrumentation, loss factors, flow factors

Table of Contents

Note to Reader

Introduction

Design and Construction

 Loop Design Considerations

 Electronic Control of Fluid Flow

 Gas Handling

 Safety Considerations

Materials Test Equipment

 Commercial Corrosion Test Samples

 Corrosion/Erosion with Orifices

 Pipe Wall Thickness Measurement

 Device Loss Factor Measurement

 Other Configurations

Apparatus Monitoring System

 System Block Diagram

 Routine Structure

 Data Acquisition

 Emergency Safety Features

 SMTP Communication Updates

 Challenges

Performance and Calibration

 Turbulent Fluid Flow

 Effect of Backpressure

 Laminar Fluid Flow

 System Equilibrium Temperature

 Heat Exchanger Performance

 Fluid Temperature at Sample

 Thermal Properties of the Loop

 Loop Component Loss Factors

 Experiment Loss Factors

 Effect of Backpressure (reprise)

 Gas Regulation

Scalability

Conclusions

Acknowledgements

Appendices

 I. Compact DAQ-9188 Modules

 II. AMS Subroutine Descriptions

 III. Least squares fits to observed data

 IV. Flow factors and loss factors

 V. List of acronyms, alloys, pipe sizes

 VI. List of Variables

References

Note to Reader

This paper makes extensive use of hyperlinks. All hyperlinks are blue, by convention, with the exception that the underlines have been removed to improve clarity of the text. At the highest level, each section in the table of contents (TOC) is linked to the referenced section. Additionally, within the manuscript each section title is linked back to the TOC. Many of the graphs of experimental data require least squares fits to the observed data. To eliminate clutter on the graph, the least squares equations have been collected in a single table in Appendix 3. Each graph is linked to the table and each equation has a return link to its respective graph, thus allowing the reader to examine the equations at will and return to the graph without thumbing through numerous pages of text. In several locations, references (and accompanying links) are made to related sections of the paper but there are no return links to the original location. Finally, we have provided external links to all of the vendor-specific information and to numerous of the References. We hope that these links make it easier for the reader to navigate within the details of the paper.

Introduction

Materials dynamically interact with their environment with serious consequences for those that are employed in harsh environments. Industries that involve materials for applications such as gas and oil pipelines, nuclear power plant coolant loops, and naval heat exchangers and propellers present highly aggressive conditions that degrade materials significantly. Due to the nature of these applications, degradation poses both hazardous conditions to human health and huge financial stresses for systems monitoring and upkeep. While some materials may be nearly inert to a specific environment, many form a protective passivation layer as an environmental response to retard further degradation. There is a complex synergistic response that involves both electrochemical interactions at the molecular level and mechanical interactions between a material and its environment at a macroscopic level. In aggressively oxidizing or abrasive environments, this passivation film may be completely removed; the adhesion between the passivation film and the substrate is often the point of failure. Many such mechanisms may be considered to be yet another form of tribocorrosion that can be added to the list provided by Ponthiaux, Wenger, and Celius (2012).

Worldwide, there are a few systems that have been developed to study materials degradation from either the electrochemical or the mechanical abrasion perspective (e.g., Det Norske Veritas; Idaho National Laboratory; Institute for Energy Technology Norway; Massachusetts Institute of Technology; Oak Ridge National Laboratory; Ohio University;

University of Michigan; Universiti Teknologi PETRONAS (UTP); University of Tulsa). These facilities are major, expensive installations, constructed to serve a variety of research and industrial needs. In contrast to these facilities, the instrument described here is oriented towards developing the experimental data necessary for creating an understanding of the complex interactions of fluid dynamics, the reactant diffusion, and the growth, spalling, and regrowth of protective oxides as occurs in tribocorrosion in highly turbulent fluids. The experimental data required to study these complex interactions include characterization of both the fluid environment and material degradation from both in-situ and invasively conducted micro- and macroscopic perspectives.

It is the purpose of this paper to describe the design, construction, and performance behaviour of an instrument that fills this gap and meets these requirements. This effort builds on the preliminary experimental apparatus designed and built in our laboratory during the past several years (Cothron, Taylor, and Todoroff 2016; Cothron et al. 2017; Lones et al. 2017) and on further improvements made during the course of our current research.

Design and Construction

Loop Design Considerations

The fundamental design of the apparatus can be divided among several different categorical groups; structural, environmental housing, environmental control, experimental, and user interface. Figure 1 presents a schematic of the apparatus while Figure 2 shows associated images that illustrate the complexity and relationship between each group. With the intention of developing an environment for the understanding of the degradation of materials in a variety of aqueous media, commercially available, easily replaceable, inexpensive, and broadly corrosion resistant materials of construction were chosen. A structural skeleton of welded steel U-channel and Unistrut™,¹ allows for inexpensive, non-destructive future modifications to the apparatus to accommodate additional desired components. The structure primarily provides a platform to support the environmental housing and associated control devices, experiments, and the user interface panels and associated electronics. The environmental housing was composed of DN 50 (51 mm

¹ Unistrut, a part of Atkore International: P1000 Channel, (<http://www.unistrut.us>, accessed 15-Feb-2018).

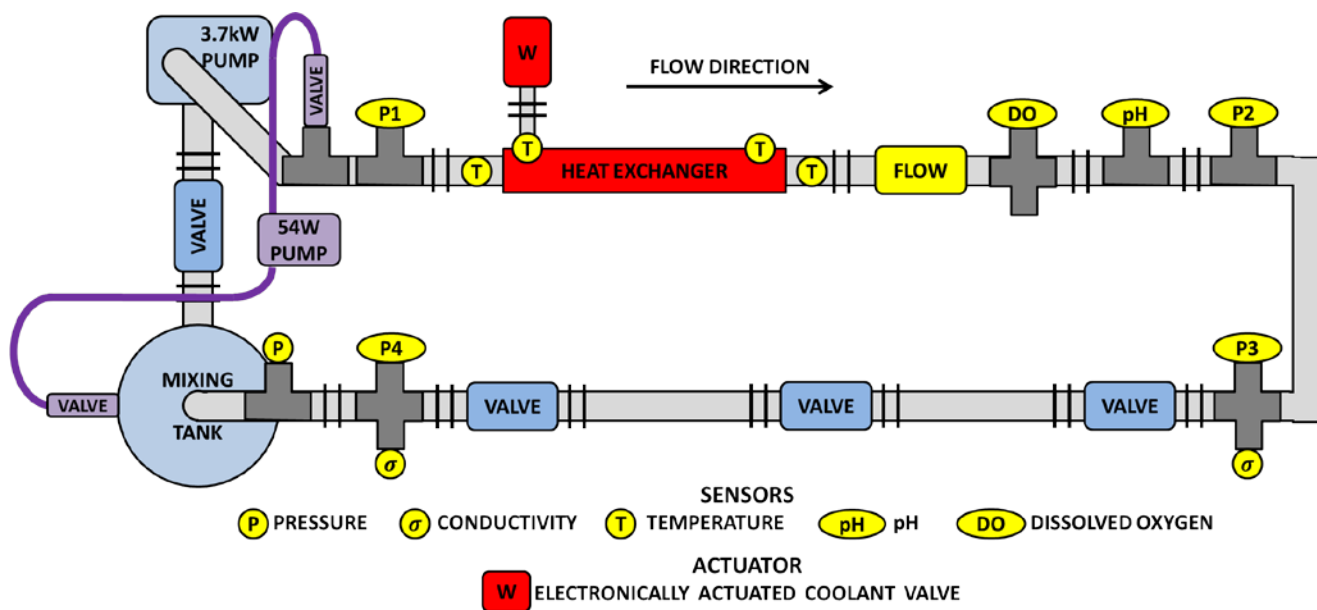
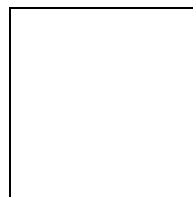


Figure 1: Schematic of the loop.



(a)

(b)

Figure 2: The Virginia Tech high turbulence corrosion loop: (a) overview of the system; and (b) view looking down the loop. Fluid enters from the lower left and returns on the right. Heat exchanger is silver tube in outbound line on left. (images courtesy LeeAnn Ellis)

diameter), chlorinated polyvinyl chloride (CPVC) pipe because of its low cost, high temperature capability, strength, ease of “welding” and high resistance to chemical attack (Boedecker Plastics; Knight).^{2,3} A total linear length of 10.8 m of pipe was utilized with commercial fittings to attach sensors and join sections. Two sections of fabric-reinforced, flexible PVC tubing reduced stress at several junctions, thus allowing for a decreased pressure drop and therefore a higher performance of the apparatus. Environmental control was composed of coupled actuators and sensors for various variables with instituted safety feedback systems (whether automated or manual). The apparatus includes two identical experimental bays installed in series that allow for a wide variety of customized experimental sections. The experimental bays are connected to the apparatus via a ball valve and union configuration, allowing for the sections to be removed easily without having to completely drain the apparatus of fluid. The user interface has both manual and computer-controlled sections. Fluid flow parameters (flow rate; temperature) are controlled via a manual control panel while an apparatus monitoring routine (AMS) allows for computer-controlled data acquisition of all environmental and material sensors remotely with emergency shutdown features instituted.

For turbulent flow, the fluid is pumped from a 38 L stainless steel mixing tank by a six-vane impeller that is driven by a 3.7 kW, 3-phase 247 V (5 HP) motor.⁴ The mixing tank, to which the recirculating fluid is returned, is a custom-made stainless steel tank with four ports for the connection or insertion of (i) the impeller pump, (ii) a 3 kW heating element, (iii) a 54 W diaphragm pump for to provide low-velocity laminar flow, and (iv) a drain valve from which fluid samples for chemical analysis may also be taken.⁵ Power for the main pump motor is provided by a 15 kW autotransformer. The angular velocity of the motor is controlled by a 7.5 kW AC variable frequency drive (VFD) that allows pumping speeds from

² See, e.g., PVC Pipe Supplies, Olive Branch, MS; (<https://pvcpipesupplies.com>; accessed 01-Feb-2018).

³ Spears Manufacturing Co, Sylmar, CA: CPVC-24 Gray/Orange Low VOC CPVC Solvent Cement, Technical Specifications; (http://www.spearsmfg.com/solvent_cement_specs/CPVC-24TS%20Technical%20Specifications_web.pdf; accessed 01-Feb-2018).

⁴ American Stainless Pumps, Los Angeles, CA: Model 2SSP/C C24660B5D3F SSP/C Centrifugal Pump, (<http://www.aspumps.com/products/sspc/>; accessed 01-Feb-2018).

⁵ Indco, Inc., New Albany, IN: Model 22K1000 stainless steel mixing vat, (<https://www.indco.com/ten-gallon-stainless-steel-mixing-vat>; accessed 01-Feb-2018).

approximately 0.32 to 10 L/s.⁶ For safety of operation, the power to the motor is switched through a non-reversing definite purpose magnetic contactor that is controlled via a 24 V low-voltage circuit.

For some materials such as Cu–Ni alloys used in marine heat exchanger applications, it is necessary to pre-treat the inner diameter of the tubing under carefully controlled oxygen and laminar flow conditions to develop a corrosion-resistant oxide layer (Tuthill 1987). To accommodate such needs, a secondary 54 W diaphragm pump is installed auxiliary to the primary 3.7 kW centrifugal impeller pump (see Figure 1).⁷ A series of ball and ball check valves isolate the auxiliary pump from the primary pump, enforcing a unidirectional flow in the loop during the operation of either pump. A 0–12 Vdc, $\Delta V=0.01$ voltage regulator allows for high-resolution control of the laminar flow.⁸

Passive heating of the system due to the turbulent pumping as found at low temperatures and high flow rates is removed by a custom-designed 1.22 m long dual-pipe heat exchanger that is installed immediately following the main pump to provide active cooling.⁹ Its fluid channel is a 51 mm diameter, copper-jacketed stainless steel tube, while the exterior (coolant) channel is a 76 mm diameter concentric copper-jacketed insulated stainless steel cylinder that is cooled with 70 psi, 10 °C water. The cooling water flow is controlled from 0.0 to 0.6 L/s by an electronic valve and proportional–integral–differential (PID) controller.^{10,11} For those cases where energy must be added to achieve a desired

⁶ Hitachi America Ltd., Industrial Components and Equipment Div., Tarrytown, NY; Model WJ200–75 10 HP AC variable frequency drive (VFD), (<http://www.hitachi-america.us/ice/ac-drives-inverters/wj-200-series>; accessed 01–Feb–2018).

⁷ Pentair SHURFLO, Costa Mesa, CA: Model 8009–541–236 12V_{dc} Diaphragm pump, (<http://shurflo.com/industrial-products/electric-diaphragm-pumps/9-8000-series-diaphragm-pump-current>; accessed 08–Jan–2018).

⁸ TekPower US: Los Angeles, CA: Model TP3005T 0–30 V, 0–5 A DC regulated power supply, (<http://tekpower.us/tp3005t.html>; accessed 01 Feb 2018).

⁹ Fluid Chillers, Inc. Lansing, MI: Pipe Heat Exchanger, Model VT021816, (http://www.fluidchillers.com/index.php?option=com_content&view=article&id=9&Itemid=14; accessed 01–Feb–2018).

¹⁰ Belimo America, Danbury, CT: Model B2050VS–02+LF24–MFT valve, (https://www.belimo.us/shop/en_US/config?code=B2050VS-02%2BLF24-MFT+US&siteName=Belimo+US+Official+Site; accessed 30–Jan–2018).

temperature (high temperatures at low flow rates), a 3 kW heating element mounted in the recirculating tank provides active heating.¹²

To assure that the system pipe remains full at all times, a 0.6 m high vertical loop of CPVC flexible tube was inserted between the downstream pressure gage (P4) and the recirculating tank. This increased the load on the pumps by 5.9 kPa (see section on [Performance and Calibration](#)).

The system is fully instrumented as indicated in Figure 1. The fluid flow is monitored by a turbine flow meter that is mounted in-line,¹³ while dissolved oxygen, pH, and fluid conductivity sensors are mounted in bushings that are inserted into the auxiliary ports of inline tees or crosses.¹⁴ Each device has a built-in thermocouple for temperature compensation. The fluid pressure at the four ends of the straight sections is measured with three digital pressure gages and one (P2) analog Bourdon gage.¹⁵ The temperature of the fluid in the recirculating tank is measured with a platinum resistance thermometer (PRT).¹⁶ This PRT is used as the control signal for a second, independent PID controller for the

¹¹ Watlow Electric Manufacturing, Winona, MN: Model PM6C2FC-ARFCDAE EZ-Zone PM Temperature Controller, (<http://www.watlow.com/products/controllers/integrated-multi-function-controllers/ez-zone-pm-controller>; accessed 30-Jan-2018)

¹² Omega Engineering, Norwalk, CT: ARMTS-2305/208 water immersion heater, (https://www.omega.com/pptst/ARMTS2_HEATER.html; accessed 30-Jan-2018).

¹³ Omega Engineering, Norwalk, CT: Model FTB-1441 liquid turbine flow meter with Model FTB-1400-RD-A flow monitor digital display, (https://www.omega.com/pptst/FTB1400_SERIES.html; accessed 30-Jan-2018).

¹⁴ Omega Engineering, Norwalk, CT: Model DOE-45PA dissolved oxygen sensor with Model DOTX-45 dissolved oxygen transmitter, (<https://www.omega.com/pptst/DOTX45.html>); PHE-45P pH electrode with Model PHTX-45 pH transmitter, (<https://www.omega.com/pptst/PHTX45.html>); and CDE-45P conductivity sensor with Model CDTX-45 conductivity transmitter, (<https://www.omega.com/pptst/CDTX45.html>; accessed 30-Jan-2018).

¹⁵ Omega Engineering, Norwalk, CT: Model DPG409 digital pressure gage with analog output, (<https://www.omega.com/pptst/DPG409.html>; accessed 30-Jan-2018)

¹⁶ Omega Engineering, Norwalk, CT: Model PRCTL-2-100-A-1 platinum resistance thermometer (<https://www.omega.com/pptst/PRCTL.html>; accessed 30-JAN-2018).

heating element.¹⁷ Four type-K thermocouples are surface-mounted to the exterior of the inlets and outlets of the heat exchanger and are used to monitor its efficiency.

The loop contains two 1.52 m experimental bays as shown in Figure 1 where custom-designed experiments may be inserted inline. These bays are isolated from each other through valves in such a way that one may work on various sections of the loop or change experimental sections without completely draining the system. Design of several such modular sample chambers and experimental configurations will be described in the following sections.

The dissolved oxygen concentration is a critical variable that must be controlled, or at least measured, if one is to develop models for the corrosion of materials (Jones 1992). An appropriate gas handling system that includes the ability to bubble high-purity argon and oxygen as well as compressed air has been included in the development of the loop.

Finally, to assure safety of personnel from scalding water and electrical hazards in the event of a burst line, a series of aluminum and Plexiglas[®] shields reduce potential exposure to users.

Electronic Control of Fluid Flow

A sophisticated manual 24 V analog control system was designed and constructed for the operation of the loop. It was our conscious decision that such a system would provide maximum student safety for an instrument that is operated unattended for long periods of time in a shared academic laboratory. No attempt has been made to provide computer control of the loop safety relay system although all data acquisition is fully automated, as will be described shortly.

The main control is separated on two panels, one of which handles all of the high voltage, high power circuitry and the other of which handles the low-power logic control functions. Cable bundles run between the two panels in cable trays built into the supporting frame. The circuitry for both panels was designed using industry-standard 24 Vac analog logic relays. The power panel delivers 110 Vac power directly to some of the instruments, to a terminal strip that powers dedicated 110/24 Vdc step-down transformers required by other

¹⁷ Omega Engineering, Norwalk, CT: Model CN16PT-330 digital display controller, (https://www.omega.com/pptst/CNPT_SERIES.html; accessed 30-Jan-2018).

instruments, and to a 110/24 Vac transformer that provides power for all of the control logic. It also delivers 208 V single-phase power to the heating element and 247 V 3-phase power to the VFD and thence to the pump motor. Each power source is isolated from the building power supplies by appropriate contactors with 24 Vac coils that are controlled by off/on switches on the operator's (low voltage) panel. The heating element power is controlled by two inline solid-state relays, one in each line, such that the PID controller can switch the power off and on in fractions of a cycle.¹⁸

The operator's control panel, shown in Figure 3(a), has a main power rocker switch that arms the system by enabling the 110 V power, a switch that enables the 24 Vac power (all of the data acquisition system and the analog logic circuits), a switch to enable the power to the 3 kW heating element, and a switch to enable the power to the VFD and therefore to the primary pump motor. The rocker switch is part of the safety control system and assures that if the system loses power, it must be manually restarted.

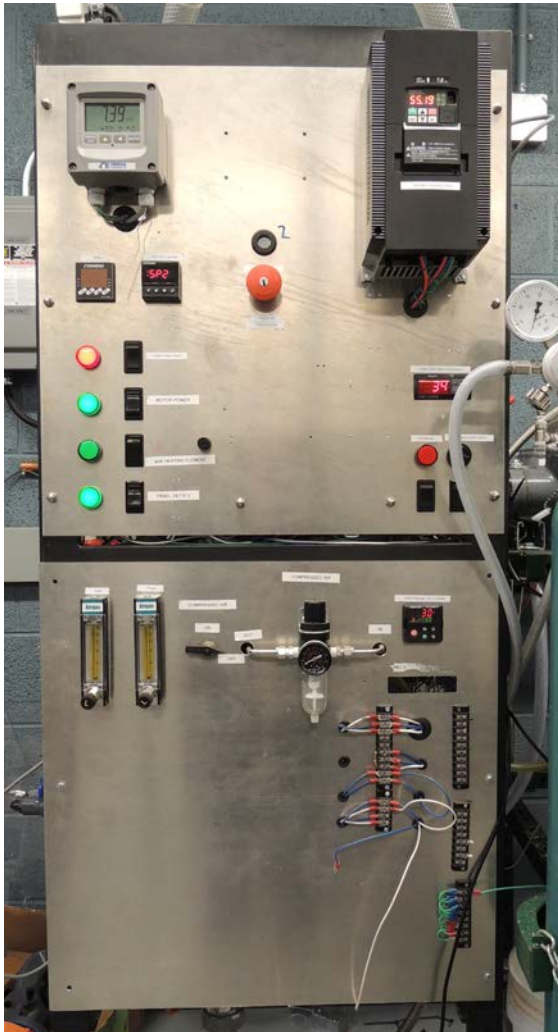
For the convenience of operators monitoring research in the experimental bays, the digital readouts for the various sensors (flow rate, dissolved oxygen, pH, and conductivity) are mounted on a third panel located between the two bays as shown in Figure 3(b). Data loggers for commercial electrical resistivity and linear polarization probes are mounted below these panels.

As research progressed, it was found that new environmental sensors were required or that some of the existing sensors failed and had to be replaced. With the data acquisition (DAQ) chassis mounted on the back wall behind the flow loop, such changes were hard to reach and difficult to make. A scheme was developed whereby all of the wiring for the 4–20 mA current loops was transferred via a cable bundle from the DAQ chassis to three terminal strips on the front of the operator's panel (e.g., see Figure 3(b)). In this manner, a sensor transmitter could be replaced in a matter of minutes by undoing three screws and withdrawing two wires from the panel.

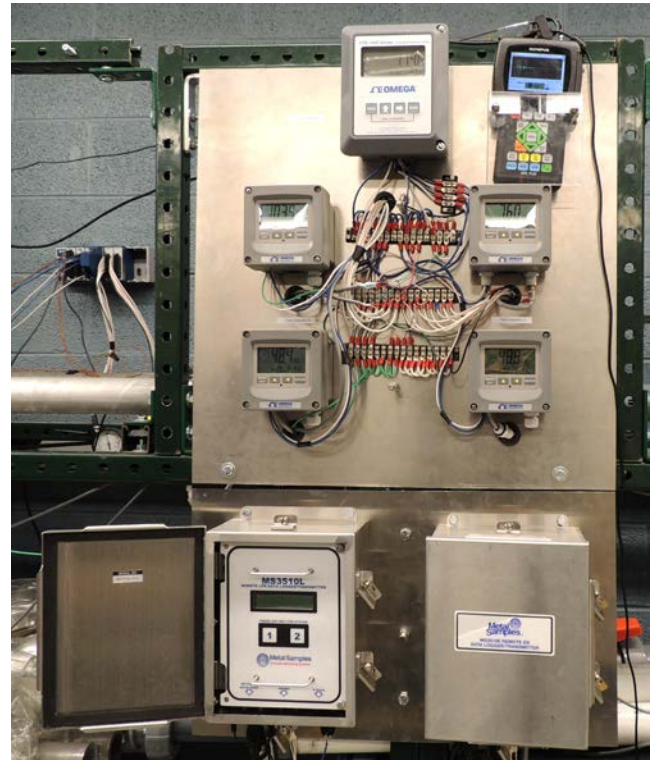
Gas Handling

All corrosion mechanisms that involve the creation of a protective passivation film depend on the concentration of dissolved species in the fluid (e.g., Jones 1992). A dissolved oxygen

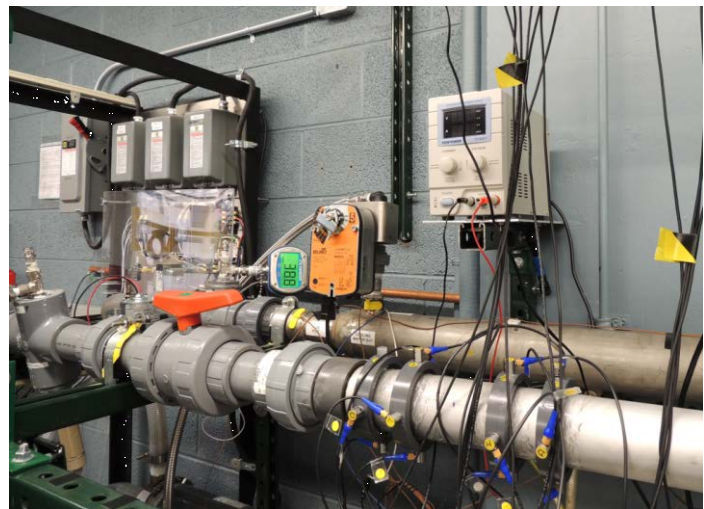
¹⁸ Omega Engineering, Norwalk, CT: Model SSR330DC50 solid-state relay with Model FHS-6 heat sink, (https://www.omega.com/pptst/SSR330_660.html; accessed 30-Jan-2018).



(a)



(b)



(c)

Figure 3: System control panels: (a) main control panel showing VFD (upper right), power switches (lower left), heater PID control (center), safety system (lower right), and argon, oxygen and air flow controllers (bottom panel); (b) fluid sensors including, from the top, fluid flow turbine and ultrasonic thickness gage

and, clockwise from the middle left, dissolved oxygen, pH and conductivity meters and (bottom) data loggers for electrical resistivity and linear polarization probes; and (c) in the foreground, an alloy pipe with ultrasonic transducers, heat exchanger with computer-controlled valve (orange), and top, auxiliary pump voltage supply. (images courtesy LeeAnn Ellis)

sensor and display is included in the fluid chemistry monitoring system as discussed above.¹⁹ A size 150A cylinder of ultra high purity oxygen with a 65 mm flow meter delivers a controlled low flow rate of gas to the surge tank (see Figure 3a).²⁰ The gas may be flowed over the surface of the fluid in the tank or delivered by a small stainless steel tube to the bottom of the tank where it is bubbled into the fluid. An identical system delivers a low, controlled flow rate of high purity argon that is used to control the partial pressure of the oxygen in the system. A controlled flow of compressed air is also provided to purge the system of argon and return the dissolved oxygen to the concentration at atmospheric conditions.

Safety Considerations

Safety of personnel and of the system can be separated into physical and engineering controls. As noted above, large safety shields protect personnel from scalding water in the event of a major burst in the loop when operating at high temperatures. Engineering safety controls have been implemented that trigger both software and hardware automated emergency shutdowns of the system.

The fluid level in the tank is monitored by an ultrasonic level detect.²¹ This device is set to assure that there is always at least 150 mm of fluid over the 3 kW heating element, thus preventing the burnout of an uncovered heater or damaging the impeller by running it dry. The recirculating tank temperature is also monitored by an externally mounted type-K

¹⁹ The specifications of the DOE-45P dissolved oxygen sensor assure us that this device operates correctly in the temperature -flow rate space of the loop.

²⁰ Airgas Inc., Radnor, PA: Model Y214651 65 mm flowmeter, (https://www.omega.com/pptst/CN700_SERIES.html), accessed 30-Jan-2018).

²¹ Omega Engineering, Norwalk, CT: Model LVU-150-R ultrasonic level sensor with Model LVM-11 level track kit, (<https://www.omega.com/pptst/LVU150.html>); accessed 30-Jan-2018).

thermocouple in conjunction with a set point controller.²² This is usually set at 80 °C, thus allowing for a 13 °C tolerance below the 93 °C maximum operating temperature for CPVC (Boedeker Plastics). However, for lower temperature investigations, the set point may be set to a temperature only 10 to 15 °C above the operating temperature, thus protecting the experiment to some extent.

The outlet pressure for both pumps is monitored at location P1 by the data acquisition system. A computer controlled, electromechanical relay is wired in series with other temperature and level detect relay switches for the apparatus, allowing the data acquisition system to trigger an emergency shutdown if an over-pressure limit is reached. Given the primary pump's operating curve, this over-pressure limit was flow-rate corrected for the apparatus (see Figure 22).

Finally, there is a large, red emergency SCRAM button in the center of the panel as seen in Figure 3(a).²³ This switch has a key lock such that the system can only be started or reset by an authorized operator. This switch may be activated in the event of cavitation or air hammer, both of which have been known to cause violent vibrations of the system. These three devices are connected in series and assure that in the event of any one of the alarms, all power is disconnected from the system and it is locked out until an authorized restart. If there is such an event, a very loud enunciator sounds and a red lamp is lit.²⁴ Such a system also assures that in the event of a building power outage, the system cannot restart automatically.

In addition to these user-designed safety features, the VFD has an internal safety feature to prevent over-current to the pump motor through an immediate shutdown. This feature protects the pump in the event that a significant back-pressure is developed resulting in the primary pump stalling.

²² Omega Engineering, Norwalk, CT: CN702 thermocouple limit controller, (https://www.omega.com/pptst/CN700_SERIES.html); accessed 30-Jan-2018).

²³ According to Wikipedia, "a SCRAM is an emergency shutdown of a nuclear reactor." We have adopted a similar terminology.

²⁴ Omega Engineering, Norwalk, CT: Model 70A-1 audible alarm enunciator, (https://www.omega.com/pptst/70A_ALARM.html); accessed 30-Jan-2018).

Materials Test Equipment

To assure modularity and ease of entry of various corrosion experiments into the loop, two identical sections, each 1.52 m long, were fitted with unions, thus providing two bays for the insertion of different experiments into the line (see Figure 1). Several compatible experimental sections have been developed that allow the tribocorrosion behaviour of a wide range of metals and alloys to be studied across a wide variety of environmental conditions. Among these are (i) an assembly that allows for the insertion of standard, commercial corrosion samples, (ii) an assembly that allows sections of pipe or tube to be exposed downstream from orifices, flow conditioners or valves, (iii) an assembly in which the wall thickness of pipes and tubes downstream from various orifices can be measured, and (iv) a device with which the differential pressure drop across various orifices of interest can be measured and thus the loss factor for each can be experimentally determined. Other devices, such as a wall shear stress monitor and a fluid flow hot film anemometer, are under development, while an in-line electrochemical potentiostat is being planned.

Commercial Corrosion Test Samples

Two commercial corrosion probes were assembled into a single experimental section with the probes spaced at a distance greater than 10 interior pipe diameters apart to ensure hydrodynamic normalization into fully developed turbulent flow. An electrical resistance (ER) probe was positioned upstream of the second probe, a linear polarization resistance (LPR) probe (see Figure 4).^{25,26} The ER probe measures corrosion through measuring the change in resistivity of a metal specimen that is mounted flush into the fluid flow. Assuming the composition does not significantly change for a 250 μm thick disk, the change in resistance is related to a change in geometry (material removal) for the specimen (Metal Samples 2018a). The LPR probe measures corrosion through measuring the polarization resistance across an anode and a cathode composed of the same material (Metal Samples 2018c). The materials, shaped as cylinders and positioned perpendicularly into the hydrodynamic flow field with one cylinder forced to become a cathode via an

²⁵ Metal Samples Co., Munford AL: Model ER3322 Electrical Resistance Probe, (<http://www.alspi.com/erprobemenu.htm>; accessed 15 Aug 2017).

²⁶ Metal Samples Co., Munford, AL: Model LP3222 Linear Polarization Resistance Probe, (<http://www.alspi.com/lprprobemenu.htm>; accessed 15 Aug 2017).



(a)



(b)



(c)

Figure 4: In-situ corrosion probes: (a) linear polarization resistance, (b) electrical resistance, and (c) the devices installed in the loop. (images (a) and (b) courtesy Metal Samples Inc; image (c) by LeeAnn Ellis.)

external power supply, forcing the counter cylinder to be an anode (Metal Samples 2018b). Each probe is connected to a data logger that is read by the data acquisition computer via a 4–20 mA current loop interface.²⁷ Images of these devices are shown in Figure 4.

A challenge with the probes was that they were mounted via commercial tees that alter the cross section significantly and thus affected the turbulence significantly. Attempts were

²⁷ Metal Samples Co., Munford, AL: Model MS3500x data logger, where X=E or L for the ER and LPR probe, respectively. (<http://www.alspi.com/erprobemenu.htm>; accessed 15 Aug 2017).

made to reduce this effect by inserting 3D printed CPVC mounts that limited to the clearance of the probe at the wall of the tube to a about 50 μm . However, flow disturbances were still present. This experimental section is normally positioned in the upstream experimental bay to normalize the incoming fluid flow.

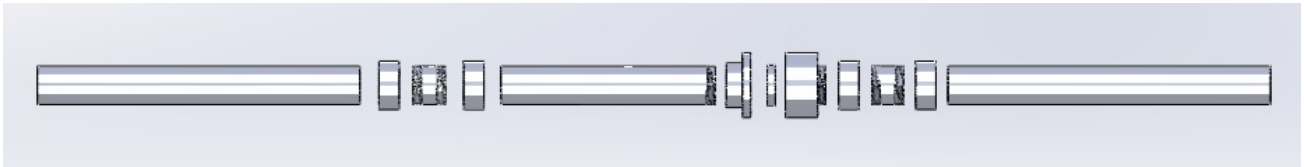
Corrosion/Erosion in the Presence of Orifices

The current research in our group primarily focuses on the effects of various devices such as valves and flow conditioners on the downstream tribocorrosion of alloy pipes and tubes. A universal sample chamber was designed to allow the insertion of custom designed orifices that simulate components of interest into the system without changes in cross section associated with transitional components. A drawing of the assembly is shown in Figure 5. A 300 mm long section of pipe/tube directly downstream of the chamber allows users to investigate the impact of different orifices on tribocorrosion phenomena. The universal sample chamber was constructed of stainless steel for durability and allowed for orifices up to 38 mm in width and 63.5 mm in diameter. The chamber is galvanically isolated from the downstream material of interest with CPVC transfer unions. In the event that a part must be longer than 38 mm, a 102 mm extension insert may be placed between the two flanges, thus allowing components up to 140 mm long.

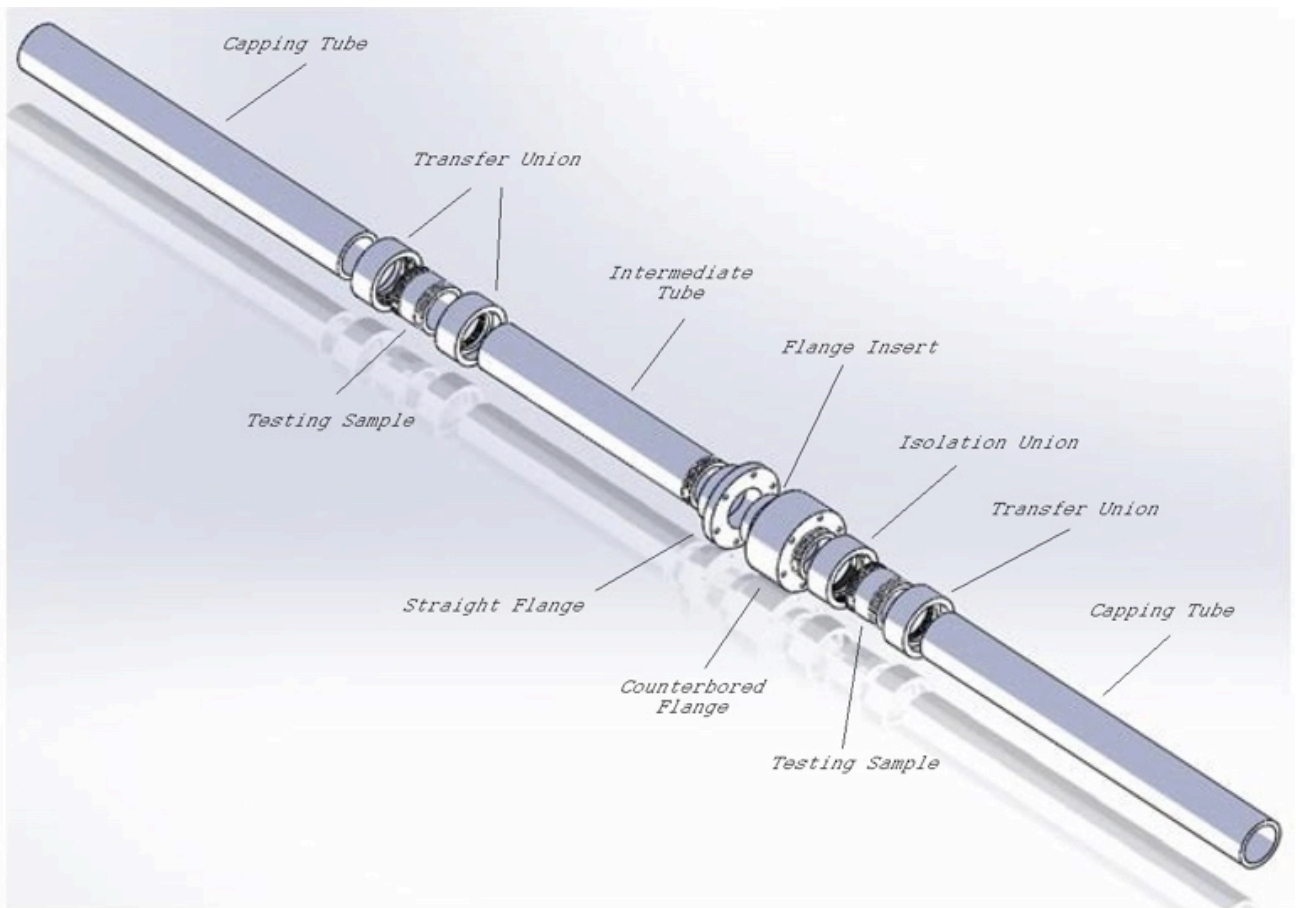
Pipe Wall Thickness Measurement

A key component of studying material degradation, or any dynamic process, is the necessity for measurements to be conducted regularly and frequently over the duration of the exposure. Such dynamic measures of material performance may be characterized by in-situ, non-interfering ultrasonic wall thickness (UT) measurements utilizing an ultrasonic transducer and an associated ultrasonic data acquisition and processing instrument.²⁸ Here, the time of flight of ultrasonic pulses is measured as the pulse is reflected from the inner and out surfaces of the tube. With a well-calibrated acoustic velocity for the specimen, the thickness is easily calculated. Accuracy, resolution, and penetration capability may be altered depending upon the frequency of the signal and which time interval is measured. For this application, 20 MHz transducers are used and the time interval between two

²⁸ Olympus Corporation of the Americas, Scientific Solutions Group, Waltham, MA: Model 38DL Plus thickness gage with optional Model DLP-HR high-resolution software, ([https://www.olympus-ims.com/en/38dl-plus/-!cms\[tab\]=%2F38dl-plus%2Fcorrosion-measurement](https://www.olympus-ims.com/en/38dl-plus/-!cms[tab]=%2F38dl-plus%2Fcorrosion-measurement); accessed 08-Jan-2018).



(a)



(b)

Figure 5: The testing module used to investigate 2024-T3 aluminum in highly turbulent seawater: (a) assembly diagram of components; (b) isometric drawing of the assembly. In the drawings, fluid flows from lower right to upper left.

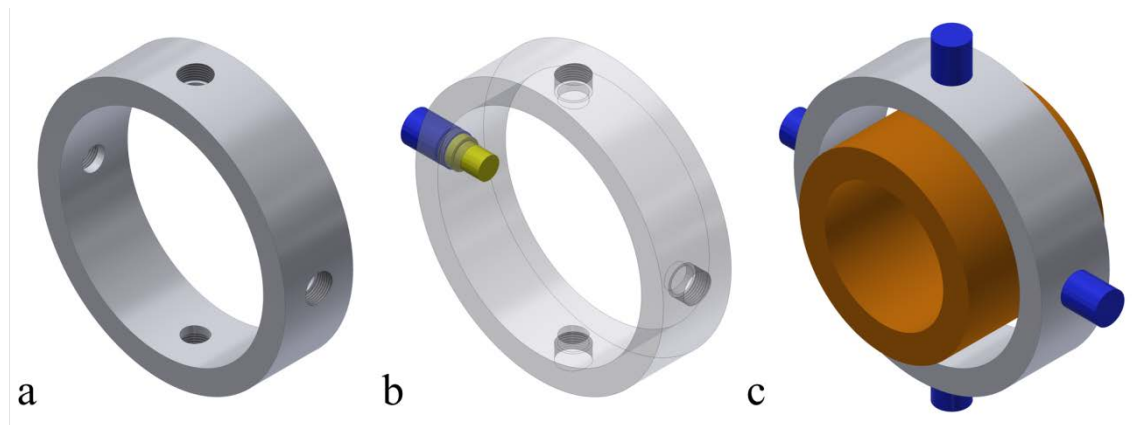


Figure 6: UT transducer adapter, shown (a) as designed, (b) transparent with a single attached UT transducer (blue) and associated delay line (yellow), and (c) completely configured around a test specimen (orange).

successive backwall echoes in mode 3, which represents one round trip test in the material, is measured, providing a resolution of $2.5\text{ }\mu\text{m}$.²⁹ Delay lines are spaced between the transducer element and the specimen, further separating the transmission excitation pulse recovery from backwall echoes to increase both accuracy and precision (Olympus Corp. 2017). Toughened PS delay lines (0.25 ms) were chosen for this application. If the passivation films on the substrate are less than about $1\text{ }\mu\text{m}$, as is often the case, passivation film thickness measurements are outside the capability of the transducers.

Custom designed UT mounts fix the transducers against the experimental test sections and thus eliminate systematic reapplication errors. The mounts were constructed from CPVC, forming 19 mm wide rings that support up to four transducers spaced radially at increments of 90° (Figure 6). Transducers thread into the mounts, pressing their required time delay lines against the experimental wall. Petroleum jelly ensured a continuous, clean, acoustic connection. With 14 constructed UT adapters, any configuration of azimuthal positions (0° , 90° , 180° , 270°) could be measured with adapters incrementally positioned axially (Figure 7). By convention, the 0° positions were positioned vertically with subsequent positions following the right-hand rule. The axial position of a device is determined by defining the origin, typically at the exit face of an orifice. These dimensions thus determine

²⁹ Olympus Corporation of the Americas, Scientific Solutions Group, Waltham, MA: Model M208-RM 20 Mz single element transducers with Model DLH-1 delay lines, (<https://www.olympus-ims.com/en/transducers-and-accessories/>; accessed 06-Jan-2018).

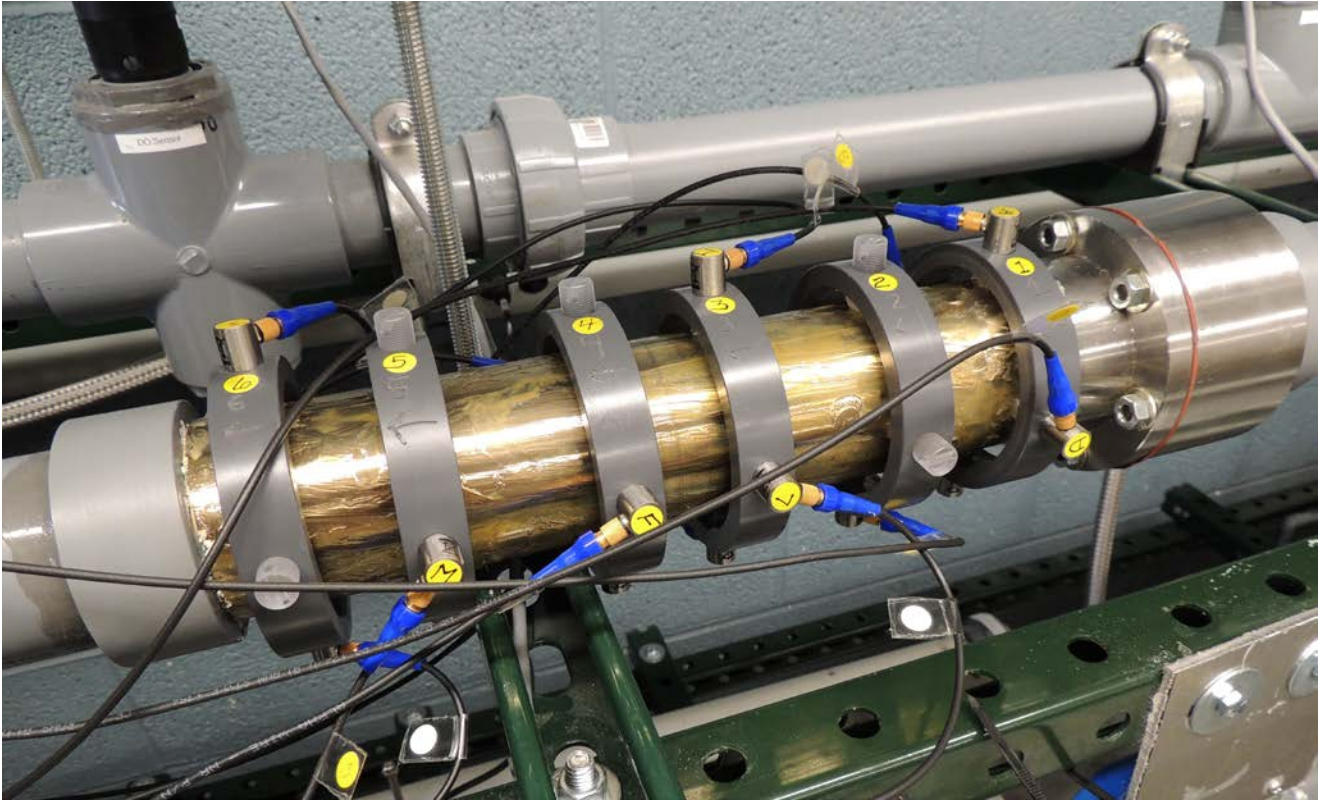


Figure 7: UT transducer adapters (labelled 1 through 6 on top) with transducers (labelled A through O) and clear plastic set screws mounted on an experimental section of nickel aluminium bronze pipe assembly. Fluid flow direction is from right to left. An orifice that simulates a valve is mounted in the stainless steel chamber on the right. (image courtesy LeeAnn Ellis)

θ and z in a cylindrical coordinate system. The transducers are labelled alphabetically A–O and adapters chronologically 1–14 with the smaller character configurations upstream. Nylon fixing bolts held delay lines in place when a full adapter configuration was not desired. The quantity and temporal spacing of UT measurements were limited by the maximum capability to switch the transducers to a common instrument and physical proximity interference between transducers during mounting and setup. Each transducer is switched and connected to a common UT instrument via a 15-input multiplexer, thus

allowing for sequentially conducted thickness measurements to be performed in a 300 s cycle.³⁰ Details of the software routine are covered in an ensuing section of the paper.

To achieve maximum accuracy in our wall thickness measurements, a calibration tube with a step in the inner wall diameter has been designed. Typically, such tubes are 250 mm long and 50 to 64 mm OD with wall thicknesses of 5 to 6.5 mm and are constructed of the same raw material as the experimental test sections. Using sections of the same tube as that under investigation assures that the calibration of the velocity of sound in the material is affected identically by the microstructure and by the parallax effects of the interface between the transducer delay lines and the outer diameter of the specimens. One half of each of these tubes is precision machined to have an ID that leaves a wall thickness of approximately 1 mm. The inner diameters of the thick and thin wall sections are measured with a precision dial bore gage to $\pm 0.3 \mu\text{m}$ while the OD is similarly measured with a precision outside micrometer to the same tolerance.^{31,32}

Device Loss Factor Measurement

The performance of various orifices, valves and flow straighteners inserted into the universal sample chamber are predicted via computations with a strong literature basis. However, it is still necessary to measure the actual performance of a device in-situ. A differential pressure gage was installed following proper ASME standards at locations of D upstream and D/2 downstream of the orifice of interest utilizing a separate, custom designed differential pressure chamber (ASME 2004, 2007). The chamber is configured with spacers to position an orifice at the correct location with respect to a defined origin and accommodates different device thicknesses. A schematic of this assembly is shown in Figure 8. For any orifice or flow conditioner of interest, there are three components: (i) a main housing that carries the fittings for the differential pressure gage and holds the device

³⁰ Linkbone, Wieruszow, PL: Model 1-to-15 Dual BNC Switch, (<http://linkbone.com/product/bnc-switch-remote-1-15/>; accessed 08-Jan-2018).

³¹ Mitutoyo America, Aurora, IL: Model 511-752 dial bore gage, (http://www.mitutoyo.com/wp-content/uploads/2012/11/2005_BoreGage.pdf; accessed 08-Jan 2018).

³² Mitutoyo America, Aurora, IL: Model 101-120 outside micrometer, (<http://ecatalog.mitutoyo.com/Outside-Micrometers-Series-101-C1094.aspx>; accessed 12-Jan-2018)

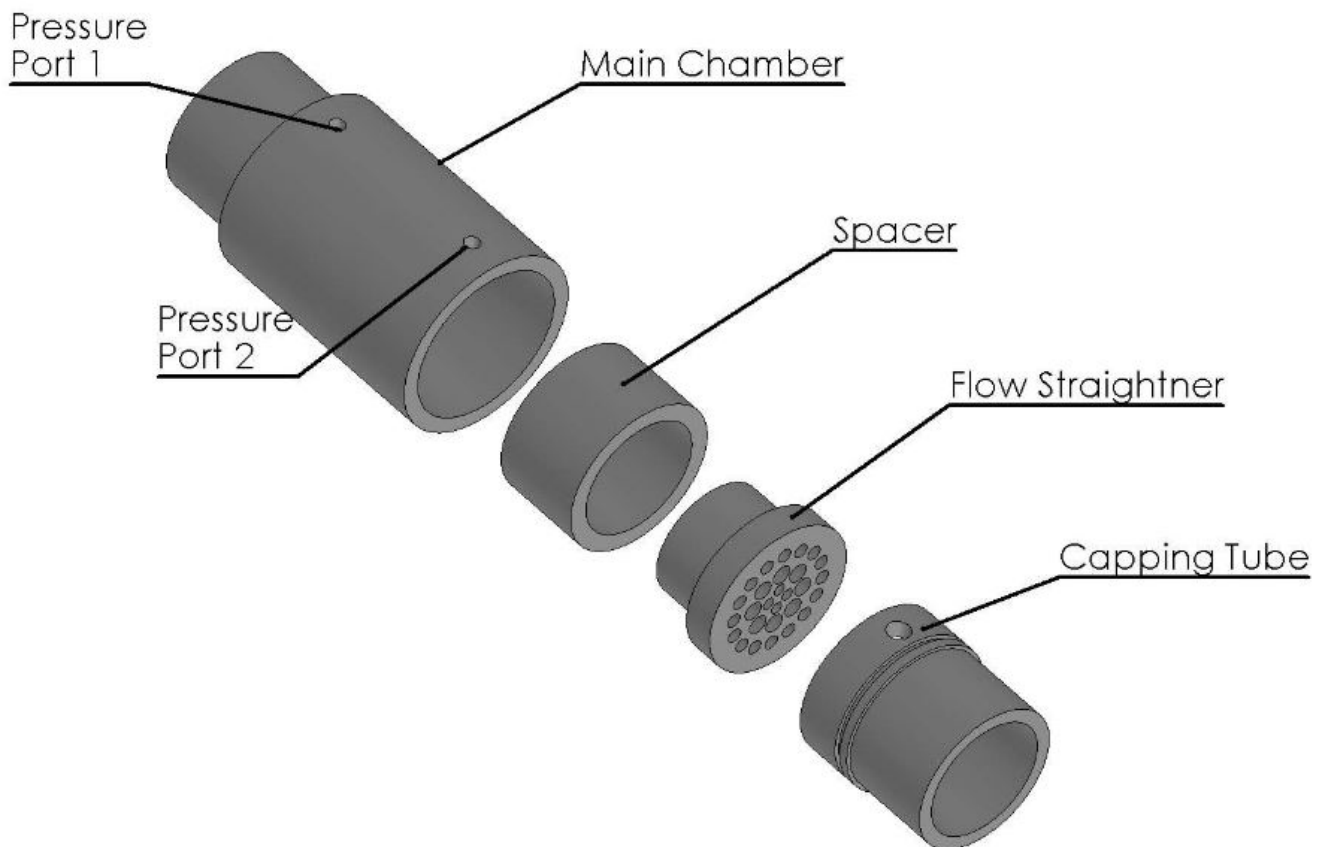


Figure 8: Schematic of differential pressure device for determining loss factor for various orifices and flow straighteners.

under test (DUT), (ii) a series of various sized spacers that are machined to assure that the face of the DUT is at the location required by the ASME Standard and (iii) a capping tube (ASME 2001). The two pressure ports are monitored by a digital differential pressure gage.³³ The analysis of data from this device is discussed in the section on [loss factors](#).

Other Configurations

To fully characterize the fluid flow in the system described here, we are developing (a) a device for directly measuring the wall shear stress using the techniques described by Schetz (2010) and Meritt and Schetz (2016), and (b) an interface that makes it possible to traverse

³³ Omega Engineering, Norwalk, CT: Model DPG409-030DWU differential pressure gage, (https://www.omega.com/pptst/DPG409_DIFF.html; accessed 30-Jan-2018).

miniature thin film anemometer probes across the diameter of the tube and to thus provide a direct measure of the orthogonal velocity components of the fluid flow and thus to provide the degree of fluctuation of the Reynolds number at a given point in the flow stream (Jorgensen 2002). The details of these devices are presented by (Todoroff 2018). An inline electrochemical potentiostat is also planned.

Apparatus Monitoring System

An apparatus monitoring system (AMS) has been developed for remote and frequent data acquisition (DAQ) of environmental conditions and ultrasonic thickness measurements, to conduct emergency shutdown procedures (ESP), and to periodically communicate status and recorded data updates with the operating user. The AMS was primarily designed around the National Instrument CompactDAQ chassis platform which allows for several simultaneous analog I/O, digital I/O, and counter/timing measurements utilizing the associated LabVIEW virtual environment and visual programming language.³⁴ The routine was written LabVIEW, version 17.0f2 (64-bit) operating on Windows 7 Enterprise.³⁵

System Block Diagram

A block diagram of the data acquisition system is shown in Figure 9. The outputs of the DOTX-45, PHTX-45 and CDTX-45 series of data transmitters used to display and record the output of the dissolved oxygen sensor, the pH sensors, and the electrical conductivity sensors, respectively, as well as the output from the fluid flow turbine, the strain gage outputs from the wall shear stress apparatus, the data loggers for commercial corrosion probes, the absolute pressure gages P1 through P4, and the differential pressure gage used to determine loss factors are all recorded via industry standard 4–20 mA current loops. Up to 24 channels of data are acquired from these instruments via three 24-bit I/O modules mounted in a compact chassis.³⁶

³⁴ National Instruments Inc., Austin, TX: The NI Platform, (<http://www.ni.com/en-us/innovations/platform.html>; accessed 09-Jan-2018).

³⁵ National Instruments Inc., Austin, TX: Model cDAQ-9188 compact DAQ chassis (<http://www.ni.com/en-us/shop/select/compactdaq-chassis>; accessed 09 Jan 2018).

³⁶ National Instruments Inc., Austin, TX: Model NI_9203 C-series current input module, (http://www.ni.com/pdf/manuals/374070a_02.pdf; accessed 30-Jan-2018).

All four of the thermocouples mounted on the heat exchanger, as well as up to twelve more thermocouples located strategically throughout the system are recorded with a 16-bit 16-input thermocouple module with built-in cold junctions.³⁷ This allows the efficiency of the heat exchanger to be measured and thermal losses of the system to be determined.

The control voltage of the Belimo heat exchanger valve as well as the control voltage for the auxiliary laminar flow pump are recorded with a four input voltage module.³⁸ A signal to the SCRAM shutdown system described above is provided by including a software-controlled relay that is in series with the level detect and the surge tank over-temperature relays.³⁹ This relay is opened under software control in the event that the pressure at P1 becomes too large and thus provides an additional level of safety for the main motor and impeller. This pressure is currently set at 200 kPa (absolute).

Finally, the multiplexor by which the various ultrasonic transducers are selected for reading and processing and the ultrasonic thickness gage both have RS232C interfaces to the computer via a USB to dual RS232C interface.⁴⁰ This interface allows us to select any one of up to 15 transducers in the array described above and read the tube wall thickness at the location of the selected transducer, all under program control and without user intervention.

The “mini chassis” communicates with the computer via a CAT-5 Ethernet cable and all data acquisition software is written in the LabVIEW[®] programming language which automatically records the data to a comma separated variable (CSV) spreadsheet file.⁴¹ The program uses

³⁷ National Instruments Inc., Austin, TX: Model NI-9213 C-series temperature input module (http://www.ni.com/pdf/manuals/374916a_02.pdf; accessed 30-Jan-2018).

³⁸ National Instruments Inc., Austin, TX: Model NI-9201 C-series voltage input module, (http://www.ni.com/pdf/manuals/373783a_02.pdf; accessed 30-Jan-2018).

³⁹ National Instruments Inc., Austin, TX: Model NI-9482 C-series relay output module, (<http://www.ni.com/pdf/manuals/373948b.pdf>; accessed 09-Jan-2018).

⁴⁰ National Instruments Inc., Austin TX: Model USB-232/2 Serial Interface Device, (<http://www.ni.com/en-us/support/model.usb-232-2.html>, accessed 10-Jan-2018).

⁴¹ National Instruments Inc., Austin, TX: What is LabVIEW? (<http://www.ni.com/en-us/shop/labview.html>, accessed 5-Feb-2018).

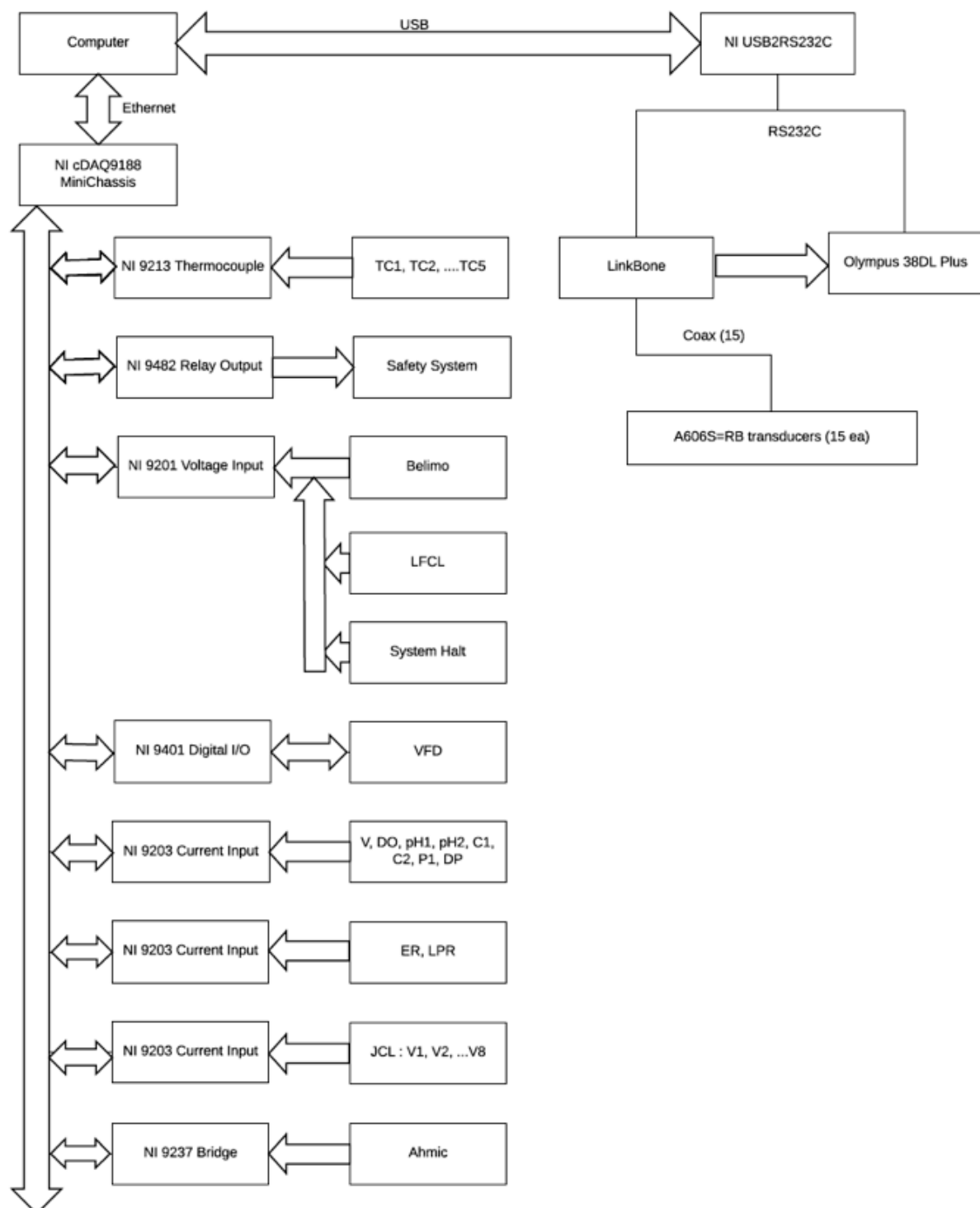


Figure 9: Block diagram of data acquisition system.

built in DAQ virtual instruments to start recording data and set the time interval between readings. Further details of the DAQ modules are given in [Appendix 1](#).

Routine Structure

The AMS utilizes an evenly stacked, hierarchal, routine structure to improve user navigation and ease of use by executing several nested and concurrent subroutines as shown in Figure 10. The AMS routine structure executes three sequential sections: Section A initializes user defined parameters from a virtual user interface (Figure 11) and stores them to local variables; Section B performs all necessary procedures for (i) DAQ, (ii) ESP, and (iii) communication updates in a timed loop structure. Sequence Section C sends an SMTP (simple mail transfer protocol) email to notify the operating user that the AMS routine has ended and attaches the DAQ spreadsheet in xlsx format. LabVIEW protocol dictates that all procedures run from left to right, requiring all signals to be present before conducting a procedure.

Data Acquisition

Data are taken from two primary sources; the NI CompactDAQ chassis platform and the UT system as shown in Figure 9, executing sequentially in a timed loop at a user defined frequency entered in Section A, referred to as the DAQ cycle. Environmental sensors are recorded simultaneously via the NI CompactDAQ chassis that features eight module slots, allowing for a wide variety of measured fluid and environmental conditions (see Figure 9). The UT system switch connects each of the 15 UT transducers to a common UT instrument via an RS232 serial commanded multiplexer which allows for sequentially conducted thickness measurements. The arithmetic mean, standard deviation, skewness, and kurtosis values for both the environmental conditions and the UT measurements were calculated and recorded from 200 and 5 measurements taken at $\Delta t=0.1$ s and $\Delta t=3$ s apart, respectively (e.g., Miller and Freund 1977, 72–74). At the end of the DAQ cycle, measurements were time-stamped, counted, and appended to a common data file. The minimum cycle period was 300 seconds. A typical e-mail message to the user on normal completion of a data acquisition cycle is shown in Figure 12(a) while a section of the attached data file is shown in Figure 13 as it would appear in MS Excel.

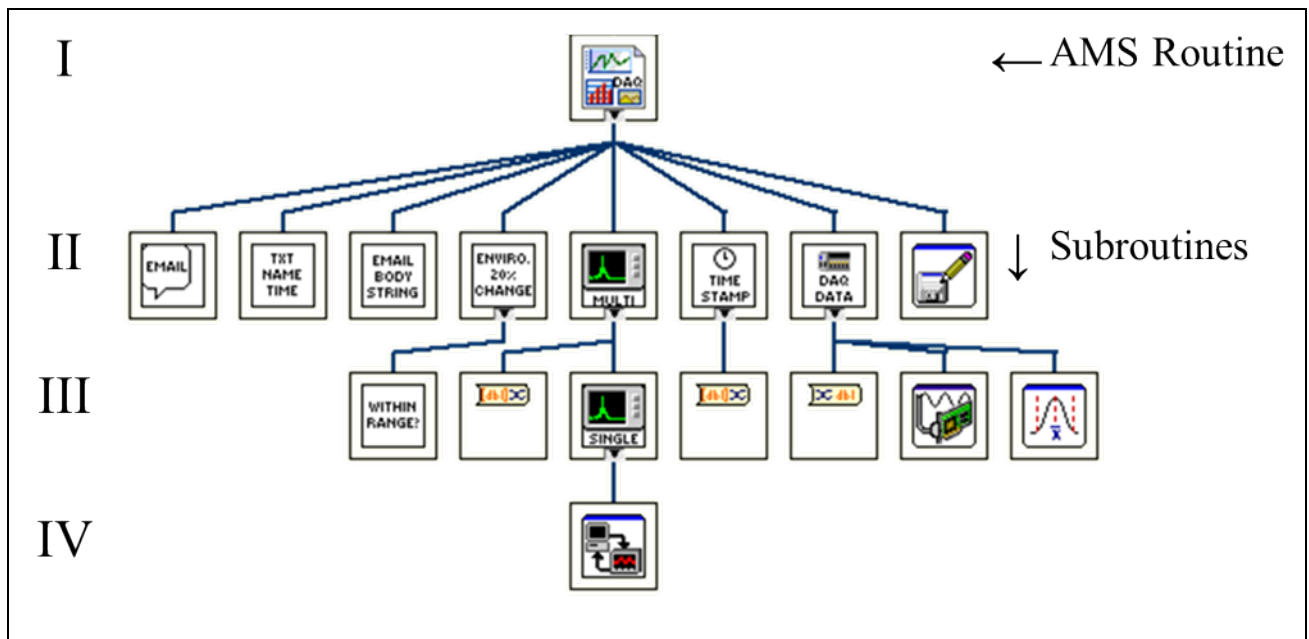


Figure 10: AMS routine and subroutine hierarchy (NI LabVIEW). The various subroutines that are run at each level (I,..IV) are described in Appendix 2,

USER INFORMATION	START
User <input type="text"/>	<input type="button"/> <input type="button"/>
Email Address <input type="text"/>	DAQ INFORMATION
Material <input type="text"/>	Kill DAQ <input type="button"/> DAQ Iteration Count <input type="text" value="0"/>
Condition <input type="text"/>	<input type="button"/> Program will execute a full DAQ iteration before ending.
Trial # <input type="text"/>	Update SMTP Period (s) <input type="text" value="0"/>
	DAQ Period (s) <input type="text" value="0"/>
	UT Sensor Quantity <input type="text"/>

Figure 11: AMS routine User Interface (NI LabVIEW)

----- Forwarded message -----

From: <vthtcl@gmail.com>
Date: Fri, Feb 16, 2018 at 10:40 AM
Subject: Data Update - Peter - 2/16/2018 - 10:37:27 AM
To: peter007@vt.edu

This is an automated SMTP from the labVIEW data acquisition program. See experimental details below and the attached information.

USER: Peter
MATERIAL: 2024-A1
CONDITION: Testing - 10 Pa for 50 hours at 3.49 L/s (~26.58Hz), then 40 Pa for a minimum of 75 hours at 7.49 L/s (~55.19Hz). Had to add error handler to email application. Change in DAQ Period (moved from 900 to 350s) during count 83. This may take a few periods to readjust.
TRIAL: 4
START DATE: 2/14/2018
START TIME: 3:14:57 PM

For more information, contact the labVIEW author: Peter Todoroff

(a)

----- Forwarded message -----

From: <vthtcl@gmail.com>
Date: Sat, Feb 10, 2018 at 20:40
Subject: Rapid Environmental Change - Peter - 2/10/2018 - 8:36:56 PM
To: <peter007@vt.edu>

This is an automated SMTP from the labVIEW data acquisition program.
The environmental condition(s) of

Conductivity

have changed greater than 20% since the last data acquisition period

See experimental details below and the attached information.

USER: Peter
MATERIAL: 2024-A1
CONDITION: Testing - 10 Pa for 48 hours at 3.49 L/s (~26.58Hz)
TRIAL: 1
START DATE: 2/10/2018
START TIME: 8:21:56 PM

For more information, contact the labVIEW author: Peter Todoroff

(b)

----- Forwarded message -----

From: <vthtcl@gmail.com>
Date: Mon, Jan 15, 2018 at 15:15
Subject: Experiment Aborted - Peter - 1/15/2018 - 3:14:03 PM
To: <peter007@vt.edu>

This is an automated SMTP from the labVIEW data acquisition program. The data acquisition program has been aborted, whether deliberately or desired.
See experimental details below and the attached information.

USER: Peter
MATERIAL: CPVC
CONDITION: Overnight test - ensuring DAQ does not slow down.
TRIAL: 1
START DATE: 1/14/2018
START TIME: 6:20:03 PM

For more information, contact the labVIEW author: Peter Todoroff

(c)

Figure 12: Text of e-mail messages sent to user after each data acquisition cycle: (a) on normal completion of cycle; (b) on environmental change of 20%; and (c) DAQ abortion.

itself and the operating users through emergency shutdown procedures that must be reset manually.

SMTP Communication Updates

A necessary feature for a routine that acquires data remotely, frequently, and for long durations is periodic status and emergency updates. The AMS routine executes SMTP loops by emailing the operating user an attached DAQ.xlsx spreadsheet (i) during data updates at a user-defined frequency (Figure 12(a)), (ii) during emergency situations when environmental condition(s) have changed by 20% from the previous DAQ iteration (Figure 12(b)), (iii) when software error codes are generated, and (iv) once the AMS routine is aborted (Figure 12(c)). In each case, the attached file is the current.xlsx file without modification. The error code suggests where in the last few data records the user might look for the source of the potential problem.

Challenges

As user requirements and expectations changed during system development and testing, the structure and complexity of the AMS routine evolved similarly. Several challenges were presented during the process of producing the best possible routine. One consistent challenge that could not be eliminated or significantly reduced via design changes was signal noise. Data lines were shielded via grounded conduit where appropriate and were rerouted to avoid AC power lines. Furthermore, a precise calibration signal was utilized in order to determine the appropriate signal processing filter to stabilize each signal. The continued existence of noise motivated us to include online computation of statistical information of the signals; arithmetic mean, standard deviation, skewedness, and kurtosis over a large population of 200/5 data points (environmental/UT) at a frequency of 10/0.33 Hz (environmental/UT).

While far from elegant, the current AMS routine allows for reliable data acquisition and automated apparatus operation. The routine and subroutine structures involved are described in detail in elsewhere (Todoroff 2018).

Performance And Calibration

Before experimental research on the corrosion and/or erosion of materials could be performed in the instrument described above, a significant effort was required to calibrate its fluid dynamics performance. Among the measurements necessary were: (i) calibration of

the volumetric flow rate of the fluid as a function of VFD frequency and experimentally caused backpressures; (ii) determination of the passive heating curve due to generation of energy in the fluid by the impeller and which delineates the boundary between the conditions at which heat needs to be added or removed to reach a desired temperature at each flow rate; (iii) the thermodynamic performance of the heat exchanger and of the CPVC piping system; and (iv) the effects of backpressure on the fluid flow caused by orifices, flow straighteners and valves used in the sample chamber. Each of these is discussed in this section.

Turbulent Fluid Flow⁴²

A 1.52 m section of 102 mm diameter CPVC pipe was used in place of a sample chamber in both experimental bays and the loop was filled with distilled water. The system was operated at ambient temperature and the volumetric flow rate was recorded for various motor frequencies as set on the VFD. Measurements were made sufficiently rapidly that the fluid heating effect discussed in the next section could be ignored. This configuration assured that, with the exception of a small contribution from the smooth CPVC pipe, all flow losses were contributed by the permanent components of the system. The results are shown in Figure 14. A least squares analysis of the data shows that they fit the linear equation

$$\dot{V} = (0.156 \pm 0.001)f - (0.130 \pm 0.039) \quad (1)$$

where \dot{V} is the volumetric flow rate (L/s) and f is the VFD frequency (Hz). The $R^2 = 0.9999$ for this fit is exceptional. Eq. (2) can be inverted to give

$$f = (6.596 \pm 0.008)\dot{V} + (0.854 \pm 0.306) \quad (3)$$

which is more convenient if one wishes to acquire data at specific volumetric flow rates. The estimates of the standard error of the coefficients were determined following the analysis of Miller and Freund (1977, 295 ff).

Both the density and the viscosity of water decrease with increasing temperature (e.g., Carney and Hendricks 2017). At this time, it is not known if either has an operationally

⁴² This section is based on the work of B.M. Greenblatt (2017).

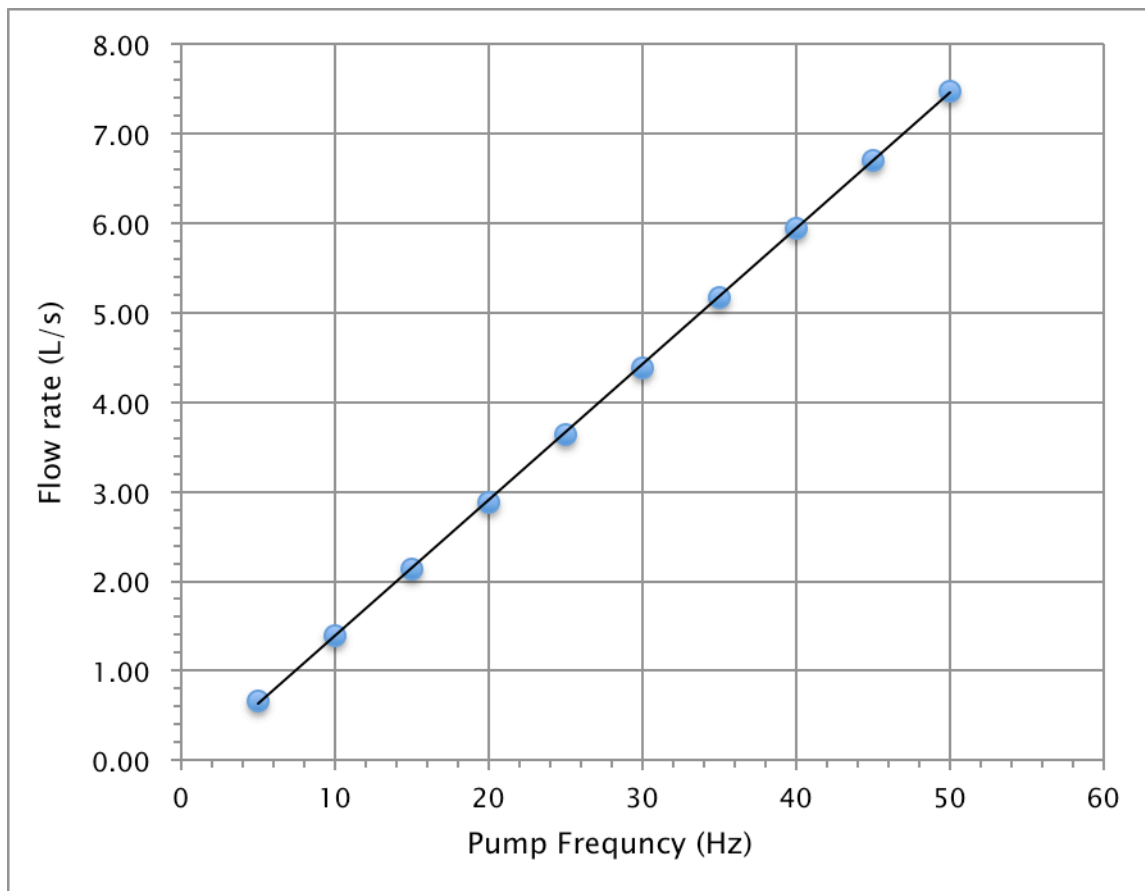


Figure 14: Turbulent flow rate (L/s) versus pump motor frequency. The least squares fit to the data is given in [Appendix 3](#).

significant effect on the relationship between the pump motor frequency and the volumetric flow rate.

Effect of Pressure on Fluid Flow

As various experiments are developed for study in the loop, the effect of restrictions and constrictions in the tubes under examination (e.g., tube diameter, the presence of orifices, flow straighteners, valves, etc.) will change the work required of the pump and will thus affect the maximum flow rate that can be achieved. Details of how these effects can be estimated quantitatively will be presented in a later section. However, to first determine the significance of such effects, a straightforward experiment was performed in which the pressure at P1 (Figure 1) was measured as a function of flow rate for various closure positions of the last ball valve in the loop just in front of P4. This ball valve was used as a

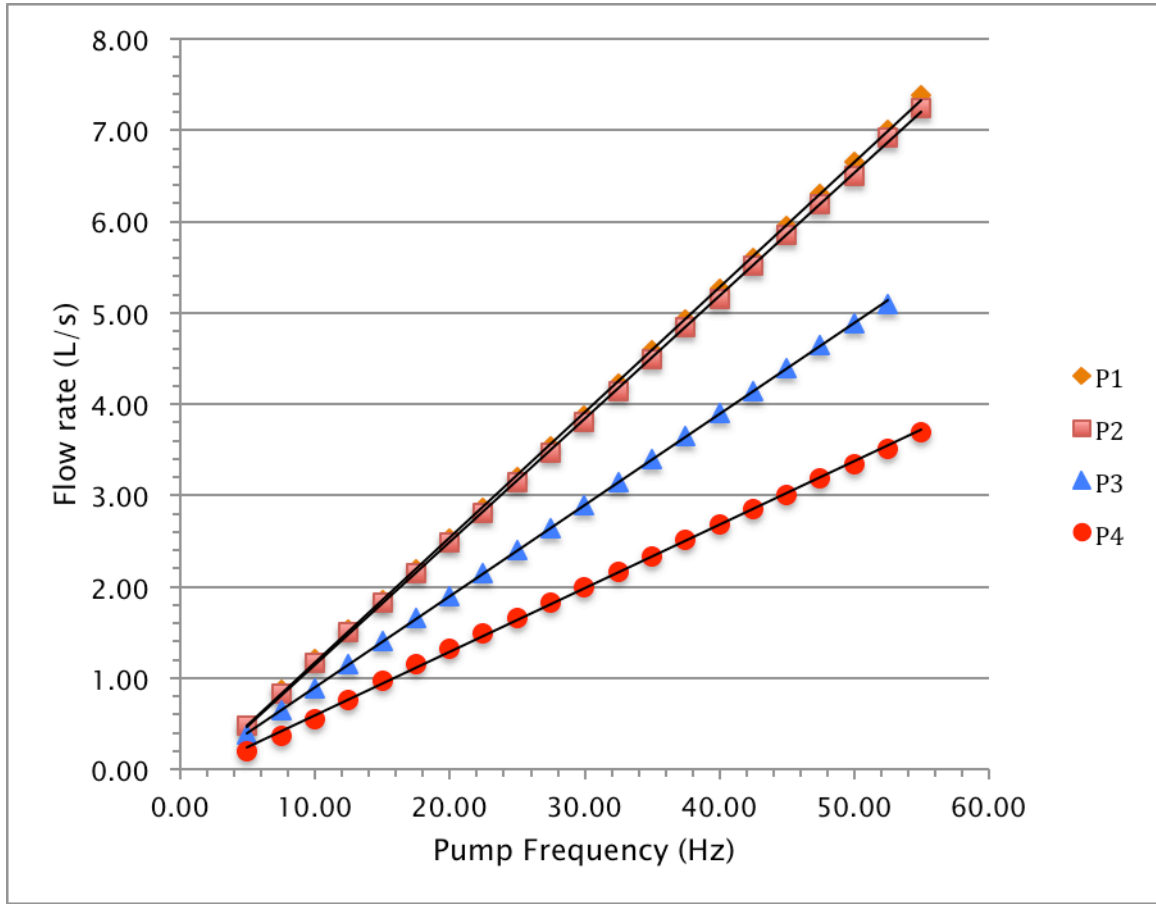


Figure 15: Effect of closing a full-bore ball valve on the flow rate of water as a function of pump frequency. P1: $\alpha=0.0$ deg. (valve open); P2: $\alpha=22.5$ deg; P3: $\alpha=45.0$ deg; P4: $\alpha=67.5$ deg. The least squares fit to the data are given in [Appendix 3](#).

proxy for various experiments in the bays to provide data for the effect of introducing a constriction into the loop. The results, shown in Figure 15, indicate a significant decrease in achievable flow rate as the valve is closed. The data in Figure 15 can be related to the flow factors, K_v , that are used to determine the maximum flow through a piping system and thence to the loss factor, K_L as will be demonstrated shortly. It is important to note that flow factors are dimensioned quantities that depend on the units of flow and pressure, while the loss factors are dimensionless. The two quantities are related inversely. Details of computations with both are given in Appendix 4. The slopes of the flow rate versus opening angle shown above are related to the valve loss factor and, as will be shown, a quantitative expression for the volumetric flow rate as a function of both the pump motor frequency and the experiment loss factor can be developed. This relationship is invaluable in designing

the operating characteristics of various experiments in such a way as to not exceed the operating point of the pump (see Figure 22).

Laminar Fluid Flow

To calibrate the laminar flow pump, the loop was set up in the same manner as described above for the calibration of the turbulent flow pump except that the valves were adjusted to allow all flow through the system to be controlled by the auxiliary pump. The flow rate was determined by measuring the volume of fluid captured in a large graduated cylinder per unit time as the flow rates were below the limit of sensitivity of the turbine flow meter. The results are shown in Figure 16. A least squares analysis of the data show that they fit the equation

$$\dot{V} = -0.0050 + 0.0042 V \quad (4)$$

where \dot{V} is the volumetric flow rate (L/s) and V is the applied voltage to the pump (volts). As in the previous section, Eq. (4) can be inverted to give

$$V = 1.19 + 238 \dot{V} \quad (5)$$

an equation that that can be more convenient if flow at a well-defined rate is desired.

System Equilibrium Temperature

Although it was anticipated that the fluid temperature would rise somewhat during long-term experiments as a result of energy deposited by the impeller, when the first experiments were run, the magnitude of the increase was much larger than expected. To quantify this effect, the system was filled with distilled water and the temperature of the water in the recirculating tank was measured as a function of time for each of four pumping speeds (flow rates): 10, 20 30, and 40 Hz (1.39, 2.88, 4.38, 5.94 L/s). The coolant flow to the heat exchanger was turned off during these measurements.

The data at the three lowest flow rates were empirically found to follow the equation

$$T(t) = T_i + (T_f - T_i)(1 - e^{-t/\tau}) \quad (6)$$

where T_i is the initial temperature of water, T_f is the final (equilibrium) temperature of water, and τ is the time constant for the process.

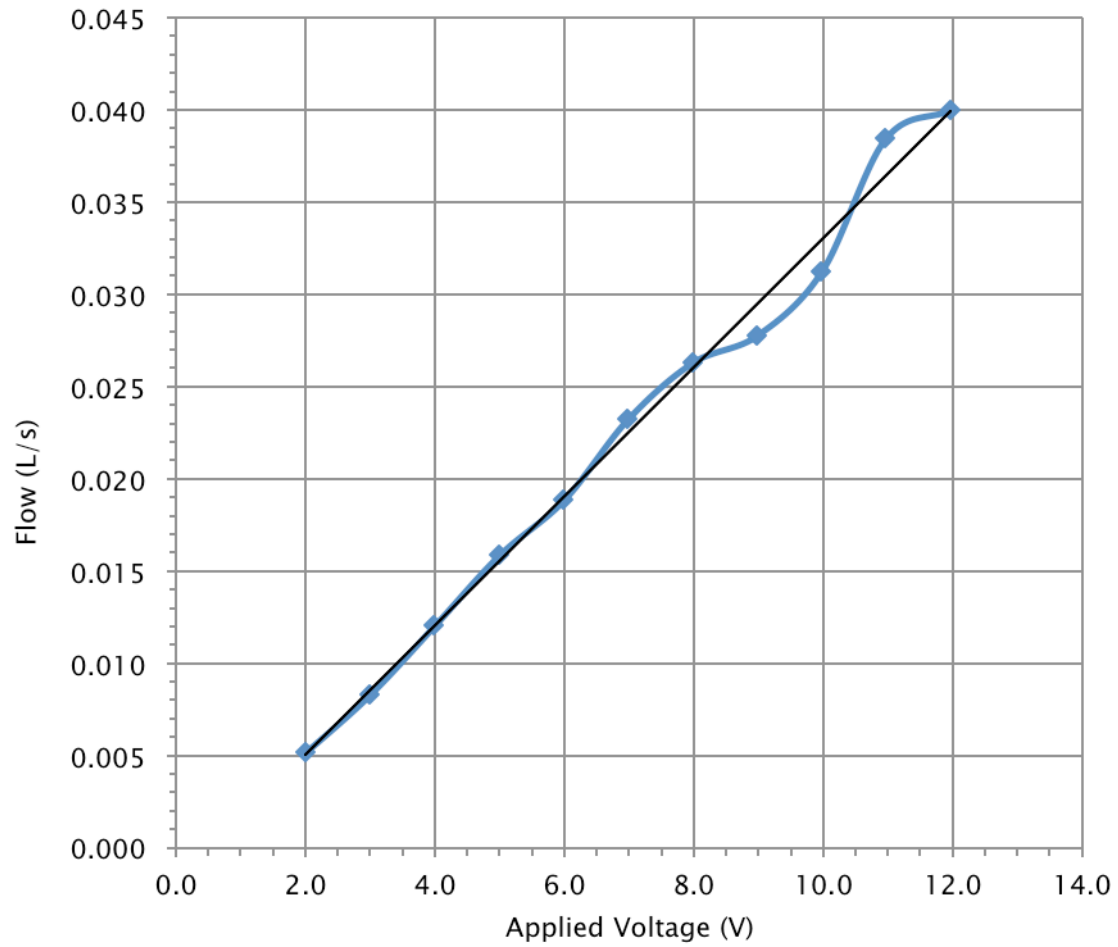


Figure 16: Laminar flow rate (L/s) versus pump applied voltage (V). The least squares fit to the data is given in [Appendix 3](#).

Eq.(6) can be rearranged as

$$T(t) = T_f + (T_i - T_f)e^{-t/\tau} \quad (7)$$

or

$$\ln\left(\frac{T(t) - T_f}{T_i - T_f}\right) = -\frac{t}{\tau} \quad (8)$$

A plot of the left-hand side of Eq. (8) versus t should be a straight line with slope of $1/\tau$. A plot of how well this relationship is obeyed is shown in Figure 17.

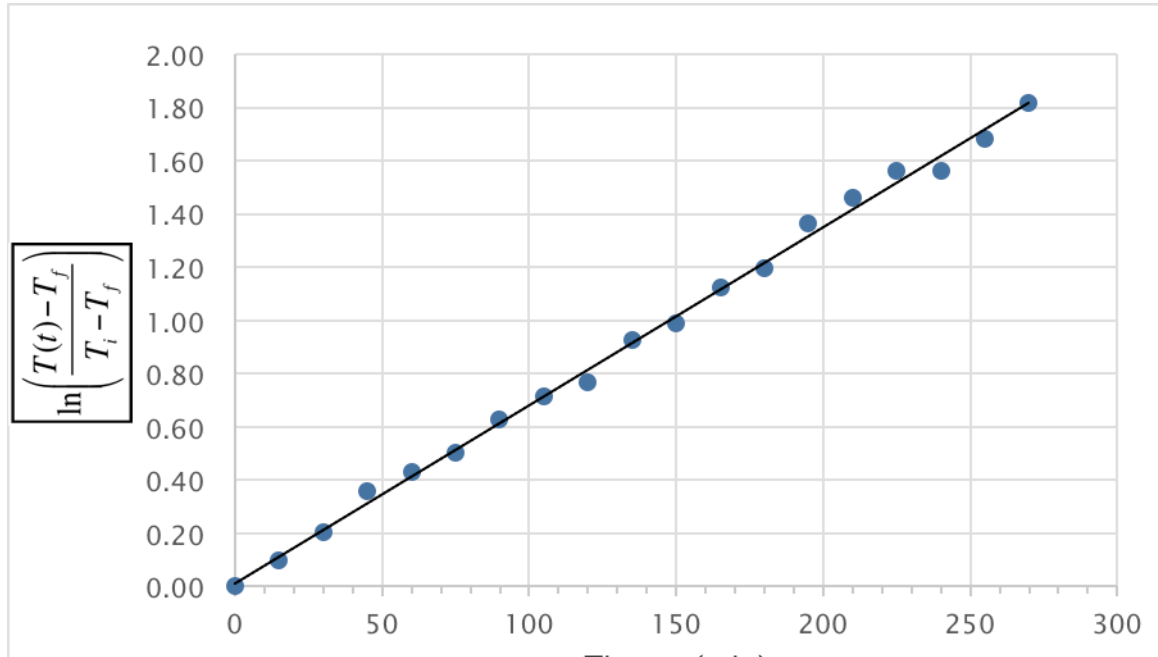


Figure 17: Plot of temperature versus time for 20 Hz run. Data are in format required by Eq. (8). The least square fit to the data is given in [Appendix 3](#).

If data cannot be recorded when the water reaches T_f , then the final temperature may be found as follows. A graph of the left-hand side of Eq. (8) versus t should be a straight line with an intercept of zero and a slope of $1/\tau$. Trial values of T_f are inserted into Eq. (8) and the values of the statistical R^2 of the fits are recorded. The value of T_f that gives the best fit (the largest R^2) is taken as the correct value. Following this procedure, a value for T_f for the 40 Hz run was obtained. The high value of R^2 indicates that Eq. (5) is a good model for describing the experimental data. The equilibrium final temperature, T_f , versus pump motor frequency is shown in Figure 18.

The slope of the curve in Figure 17 at time t is

$$\left. \frac{dT}{dt} \right|_{t=t} = \frac{(T_f - T_i)}{\tau} e^{t/\tau} \quad (9)$$

and at time $t = 0$ it is

$$\left. \frac{dT}{dt} \right|_{t=0} = \frac{(T_f - T_i)}{\tau} \quad (10)$$

Table 1: Equilibrium properties of fluid flows.

Frq (Hz)	T _i (deg C)	T _f (deg C)	T _f -T _i (deg C)	slope (deg C/min)	τ_1 (min)	τ_2 (min)	τ_{avg} (min)	P (W)
10	23.8	26.5	2.7	0.00564	73.5	75.2	74.2	15
20	24.2	35.2	11.0	0.05900	202	186	194	154
30	25.9	56.3	30.4	0.17030	170	179	174	445
40	24.6	92.0	67.4	0.39610	176	171	173	1035

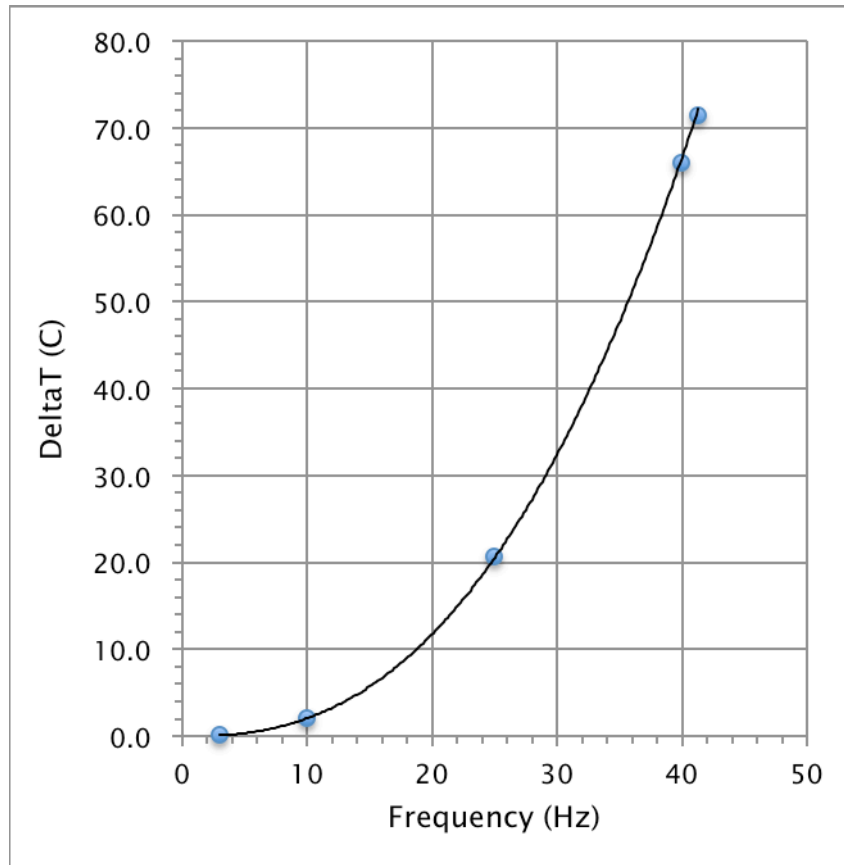


Figure 18: Equilibrium temperature rise as a function of motor frequency (flow rate). The line is the least squares fit to the equation given in [Appendix 3](#).

The time constant τ may be found from the initial slope of the heating curve, provided the final temperature of the water is known. A comparison of the values of τ obtained from Eq. (8) and from the slope of the best fit to Eq. (10) gives an indication of how well Eq. (6) fits the experimental data.

The measurement time was long enough to determine τ_f directly for the three lowest flow rates. However, it was not possible to determine τ_f directly at the highest flow rates because the equilibrium temperature was above the safe operating temperature of the system. The results of these measurements are shown in Figure 18 and are tabulated in Table 1. In the table, τ_1 is the value obtained from Eq. (8) and τ_2 is the value obtained from Eq.(10). The agreement is considered to be excellent, except for the data take at 20 Hz where they differ by an acceptable 8%.

The power dissipated by the pump may be determined as follows. At time t , the heat deposited in the water is given by

$$Q = m \int_{T_i}^T C_p dT = m C_p (T - T_i) \quad (11)$$

where Q is the energy deposited in the time required to heat the water from the initial temperature T_i to temperature T , m is the mass of fluid in the system, and C_p is the heat capacity of the fluid. It has been assumed that the heat capacity is constant over the small range of $T - T_i$. The power transferred to the water is the time derivative of Eq. (11) and is given by

$$P = m C_p \left. \frac{dT}{dt} \right|_{t=0} \quad (12)$$

The properties of water required to evaluate Eq. (12) are $C_p = 4.184 \times 10^3 \text{ J/kg-K}$ and $\rho = 992 \text{ kg/m}^3$ (Eisenberg and Kauzmann 1969). Using these values, the power dissipated in the water as a function of frequency (flow rate) may be computed from Eq. (12). The results are given in Table 1.

The increase in fluid temperature as a function of motor frequency (flow rate) shown in Figure 18 is well-explained by a power law of the form

$$T_f = T_i + 6.51 \times 10^{-3} f^{2.5} \quad (13)$$

This implies that if 80 °C is the maximum safe operating temperature of the loop and if the ambient temperature is 22 °C, the maximum frequency (flow rate) of loop operation in the absence of a heat exchanger capable of removing this excess heat is approximately 36 Hz or 5.30 L/s, values well below the design specification for the instrument. These results also show that in a configuration without a heat exchanger, it is not possible to operate the system at any temperature—flow rate combination that falls below the curve given in Figure 18.

Heat Exchanger Performance⁴³

To allow operation of the loop in the entire temperature–flow rate space, a double–pipe heat exchanger was designed and installed (Holman 2002, 511). The inner tube through which the fluid to be cooled flows is Schedule 40, type 304 stainless steel with an outer diameter of 60.3 mm and a wall thickness of 3.91 mm, while the outer tube that defines the annulus through which the coolant flows, is Schedule 10, type 304 stainless steel with an outer diameter of 88.9 mm and a wall thickness of 3.05 mm. There are six baffles in the annulus to help maximize the cooling surface area (Lawe 2017). Five type–K thermocouples were mounted on the surface of the device, one each at the inlet to and outlet from the main pipe, and one each to the inlet and outlet of the coolant annulus. An additional thermocouple was mounted on the outlet to the main pipe and was used for electronic control of the outlet fluid temperature.

For the proposed corrosion studies to be properly controlled, it is essential to know the temperature of the fluid at the sample position in the loop. This can be accomplished by interpolating between the temperatures determined by the thermocouples in the two conductivity meters. However, it is also necessary to control the fluid temperature at the outlet of the heat exchanger. Hence, it is essential to determine the difference between the fluid temperature and the temperature of the externally mounted thermocouple at the heat exchanger outlet. This calibration has been accomplished in two ways.

First, with the heat exchanger coolant valve fully opened, the flow rate of chilled (11 °C) water was measured to be 0.60 L/s at a pressure of approximately 482 kPa. Under these conditions, the fluid in the system remained at 11 °C for fluid flow rates up to approximately 6.31 L/s. The temperature at the sample position and the temperature of the

⁴³ This section is based on the work of H. A. Vanhout (H. H. Vanhout 2017).

surface of the heat exchanger were the same within experimental error. These results indicate the success of the heat exchanger design.

In a second measurement, the coolant flow to the heat exchanger was turned off and the system was allowed to come to ambient temperature. The system was then operated at a flow rate of 6.14 L/s and was allowed to come to thermal equilibrium as shown in Figure 18. The heat exchanger outer wall temperature was 65.1 °C and the ambient temperature was 23 °C. The temperature of the water flowing in the pipe may be determined from these data. The calculation proceeds as follows: (i) determine the convective heat loss from the outer surface of the pipe to the ambient air; and (ii) determine the heat loss from the flowing water to the outer diameter of the pipe by equating this loss to the convective loss computed in the first step.

The heat flux per unit length of a horizontal pipe cooled by natural convection can be determined in the following manner—first, the Grashof-Prandtl product must be determined, from which the Nusselt number is obtained, from which the heat transfer coefficient for convective heat transfer to air is found (Holman 2002, 328). The following is an example calculation for the flow conditions quoted. Other results will be reported without detail later.

The Grashof-Prandtl product is computed from

$$Gr_d Pr = \frac{g\beta(T_w - T_\infty)D_o^3}{\nu^2} Pr \quad (14)$$

where g is the acceleration of gravity (9.81 m/s²), $\beta = 1/T_f$, $T_f = (T_w + T_\infty)/2$, T_w is the temperature of the outer wall, T_∞ is the ambient air temperature, D_o is the external diameter of the pipe, ν is the kinematic viscosity of air, and Pr is the Prandtl number of air. In the present case, $T_w = 65.1$ °C, $T_\infty = 23.0$ °C, and $D_o = 60.3$ mm. For air evaluated at the film temperature, T_f , $\nu = 17.42 \times 10^{-6}$ m²/s and $Pr = 0.704$. The viscosity and the Prandtl number for air are given in Holman (2002, Table A-5, 602). For the present case, $Gr_d Pr = 6.615 \times 10^5$. The Nusselt number is then given by

$$Nu_d = C(Gr_d Pr)^m \quad (15)$$

where C and m are constants determined by the Grashof-Prandtl product. These constants are given by Holman as either $C = 0.480$ and $m = 1/4$ or $C = 0.53$ and $m = 1/4$ based on two different sources (Holman 2002, Table 7-1, 322). Using the average of these numbers, the

Nusselt number is $Nu_d = 14.4 \pm 0.7$. By the definition of the Nusselt number, the wall to air heat transfer coefficient is

$$h_a = \frac{k_a Nu}{D_o} \quad (16)$$

where k_a is the thermal conductivity of air, which, for the present case, is by interpolation in Table A-5 of Holman, $k_a = 0.0276$ W/m·K (Holman 2002, 328). For the present example, $h_a = 6.58 \pm 0.33$ W/m²·K. The thermal flux per unit length of the stainless steel pipe of the heat exchanger is thus

$$q' = \frac{q}{L} = h_a \pi D_o (T_i - T_\infty) = 52.5 \pm 2.6 \text{ W/m} \quad (17)$$

The heat loss through the wall from the flowing fluid is given by

$$q'' = \frac{q}{L} = \frac{(T_i - T_w)}{\frac{1}{2\pi R_i h_i} + \frac{1}{2\pi k_{ss}} \ln\left(\frac{R_o}{R_i}\right)} \quad (18)$$

where T_i is the temperature of the internal water of the system and is the unknown to be sought, R_i and R_o are the inner and outer radii of the heat exchanger tube, and $k_{ss} = 16.2$ W/m·K is the thermal conductivity of the 304 stainless steel wall of the heat exchanger at 100 °C (AK Steel 2013). Since the system is at thermal equilibrium, $q' = q''$.

To evaluate Eq. (18), it is necessary to know the heat transfer coefficient h_i . Expressions for h_i for turbulent water flowing through a smooth pipe have been given as a function of the Reynolds and Prandtl numbers of the fluid by Dittus and Boelter and by Gnielinski, as summarized by Holman (2002, 268). The Dittus–Boelter equation for fully developed turbulent flow in smooth tubes is

$$Nu_d = 0.023 Re_d^{0.8} Pr^n \quad (19)$$

where $n = 0.3$ for cooling of the fluid. On the other hand, the Gnielinski equation, which is valid for $1.5 \leq Pr \leq 10^4$ and $3000 \leq Re_d \leq 10^6$, is

$$Nu_d = 0.012 (Re_d^{0.87} - 280) Pr^{0.4} \quad (20)$$

For water at 65 °C flowing at 6.136 L/s) in a 52.5 mm ID smooth, Schedule 40 pipe, the Reynolds number is $Re_d = 3.39 \times 10^5$. The Prandtl number for water at 65 °C is $Pr = 2.73$

(Holman 2002, Appendix A-5, 602). With these values, the Nusselt number for the conditions of the present example is estimated to be $Nu=879$ by Eq. (19) and $Nu=1238$ by Eq. (20). The thermal conductivity of water at 65 °C is $k_w=0.659 \text{ W/m}^2 \cdot K$. With these values, and using the inside diameter of the pipe, by Eq. (16) the heat transfer coefficient at the inner wall is $h_i=10,368 \text{ W/m}^2 \cdot K$ or $h_i=14,522 \text{ W/m}^2 \cdot K$ according to Dittus–Boelter and Gnielinski, respectively.

Eq. (18) can now be solved for the difference in temperature between the fluid and the outer stainless steel wall temperature. It is found that, because the heat transfer coefficient at the inner wall is so large, the first term in the denominator of Eq. (18) is negligible compared to the second and $T_i-T_w=0.1 \text{ }^\circ\text{C}$. This difference is, for all practical purposes, negligible and the temperature reading on the externally mounted thermocouple may be taken as the internal fluid temperature.

Similar computations at other, smaller flow rates indicate similarly small temperature differences. Thus, these results show that the temperature measured by the surface mounted thermocouple at the exit of the heat exchanger is a valid control signal for the input to the PID that controls the chilled water flow for all operating conditions of the loop.

Fluid Temperature at the Sample

To be able to develop accurate models for the corrosion of metals studied in the loop, it is essential to have a good measure of the temperature of the fluid at the sample. In the absence of a thermocouple at the sample, this may be estimated as follows. The heat loss per unit length of CPVC pipe may be calculated from the relationship

$$\frac{q}{L} = \frac{T_i - T_\infty}{\frac{1}{2\pi R_i h_i} + \frac{1}{2\pi k_{CPVC} \ln\left(\frac{R_o}{R_i}\right)} + \frac{1}{2\pi h_{air}}} \quad (21)$$

where k_{CPVC} is the thermal conductivity of CPVC and all other variables have been defined. The values of h_i and h_{air} were found in the previous section and it was determined that, as an excellent approximation, T_i is given by the exterior wall temperature of the heat exchanger. For a fluid flow of 6.14 L/s of water at 65.1 °C, the heat loss per unit length of Schedule 80 CPVC pipe is 40.8 W/m. This heat must come from the fluid. The heat loss per unit length of fluid is

$$\frac{q}{L} = \dot{V} \rho C_p \frac{\Delta T}{L} \quad (22)$$

where ρ is the density of water at the fluid temperature, C_p is the heat capacity, and $\Delta T/L$ is the temperature drop of the fluid per unit length. For a flow of water at 6.14 L/s and 65 °C, the temperature drop per unit length for Schedule 80 CPVC pipe is 0.0016 °C/m.

The two conductivity sensors (see Figure 1) have built-in thermocouples that measure the fluid temperature and are used for internal temperature compensation. These sensors are separated by 4.59 m. The predicted temperature drop between the two sensors is 0.0073 °C. The measured change is 1.8 °C. This discrepancy is outside the manufacturer's statement of the precision of the two devices and is, as yet, unexplained.

Thermal Properties of the Loop

The seemingly small values of the temperature difference between that of the flowing fluid and the outer surface of the heat exchanger and the almost negligible temperature drop between the two conductivity meters must be justified. This can be accomplished by performing a system heat balance.

When operated at equilibrium with no heat added by the heating element and no heat removed by the heat exchanger, the sum of all of the losses around the loop must equal the heat input from the impeller. From Table 1, at 40 Hz (6.14 L/s) this heat input is 1034 W.

The heat loss per unit length of CPVC and stainless steel pipe (heat exchanger) were determined in the previous section. All that remains is to calculate the heat loss from the 38 L recirculating tank that is 0.36 m in diameter and 0.41 m high. The computation follows that for the heat loss from the exterior of the heat exchanger tube. For the vertical wall of the tank, the Grashof-Prandtl number is 1.358×10^8 . Also, for a vertical tank, the Nusselt number constants are $C=0.58$ and $m=1/4$ as given by Holman (2002, Table A-9, 606) and the Nusselt number is $Nu=63.7$. The resulting heat transfer coefficient for the tank surface is 4.93 W/m²·K, from which it may be determined that the heat loss from the tank is 94 W. For simplicity, we have ignored the heat loss from both ends of the tank. The tank has a polished surface for which the emissivity $\varepsilon=0.074$ that results in a radiant heat loss of 10 W (Holman 2002, 401 and Table A-410, 607). Thus, the total heat loss from the tank is estimated to be about 104 W.

The total length of the piping in the system is 11.73 m, of which 1.22 m is the heat exchanger that has only 0.23 m that is uncovered and thus loses heat to the air. The

balance is CPVC. Knowing the heat transfer coefficients for each of the surfaces, we find the total heat loss for the system is 561 W for the conditions of this measurement. This compares in magnitude with the estimated heat input of 1034 W from the impeller and validates that the computed temperature changes are realistic, but quite small.

Loop Component Loss Factors

The pressures in the piping system during pumping are critical parameters that control the maximum flow rate that can be achieved at the site where corrosion samples reside during an experiment. We have measured the static pressure as a function of flow rate at each of the four locations identified in Figure 1 with Bourdon-type pressure gages as shown in Figure 19.

The head loss for any component, be they be pipe, fittings such as elbows and valves, or in-line devices such as orifices, flow meters, or any such devices, the pressure loss can be computed from the relationship

$$\Delta P_{\text{dev}} = \frac{1}{2} K_L \rho \dot{V}^2 = \frac{8 K_L \rho \dot{V}^2}{\pi^2 D_i^4} \quad (23)$$

where K_L is the dimensionless loss factor (Munson et al. 2013, 492). In the following, we estimate the loss factor for each of the permanent components of the loop.

First, the pressure drop in CPVC pipe is calculated. Gages P3 and P4 are separated by 4.60 m of CPVC pipe. Thus, the pressure loss per unit length of CPVC is

$$\Delta P_{\text{CPVC/m}} = (P3 - P4) / 4.60 \quad (24)$$

where the pressure drop is given in kPa/m. The loss factor per meter for CPVC is then found from Eq. (23) to be $K_L^{\text{CPVC/m}} = 0.38 \pm 0.06 / \text{m}$. The large standard deviation results from the imprecise pressure values recorded from the Bourdon gages at low pressures. This value compares well with the value of $K_L^{\text{CPVC/m}} = 0.45 / \text{m}$ computed from the data from Spears (undated, 27).

Another contribution to the pressure drop in the system is that caused by the four 90 degree elbows. The loss factors for the elbows may be calculated as follows. The distance between gages P2 and P3 is 0.46 m with an elbow at each end (see Figure 1). The pressure drop across each elbow is thus

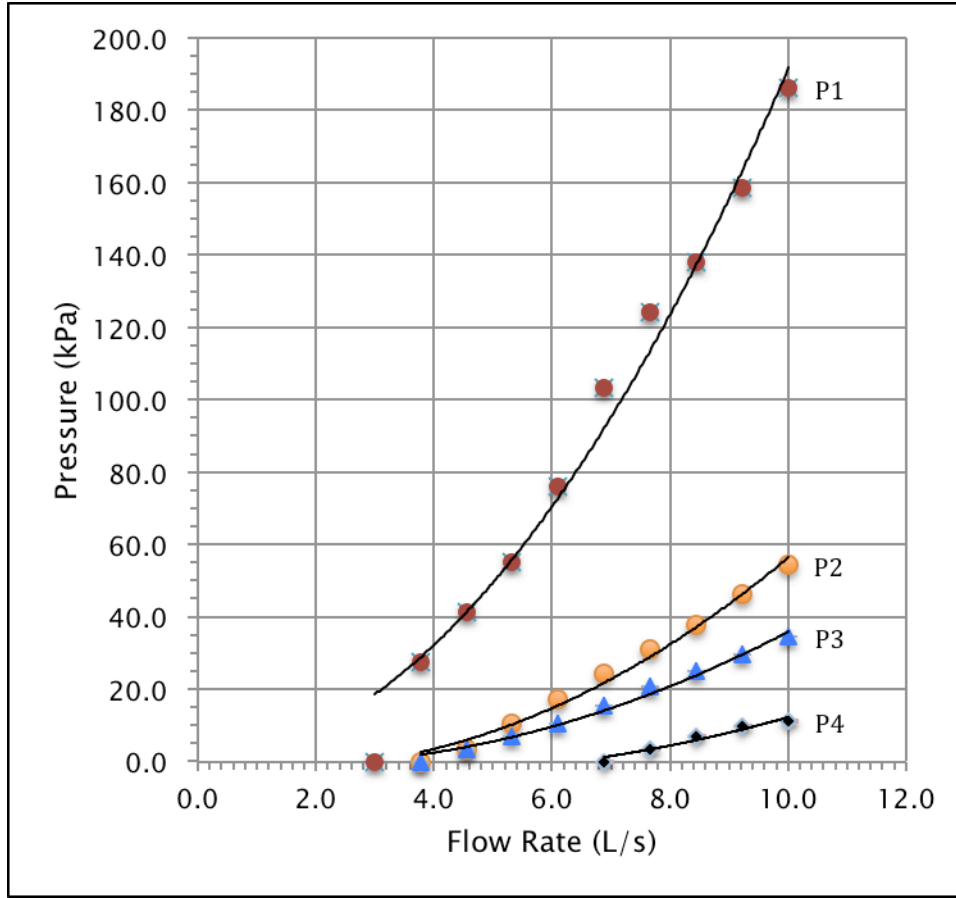


Figure 19: Gage pressure at points P1, P2, P3 and P4 shown in Figure 1. The lines are the least squares fits to the data, the equations for which are given in [Appendix 3](#).

$$\Delta P_{cl} = \frac{P2 - P3 - 0.46\Delta P_{CPVC/m}}{2} \quad (25)$$

where $\Delta P_{CPVC/m}$ is given by Eq. (24). Substitution of these data into Eq. (23) and solving for the loss factor yields the result that $K_L^{cl} = 0.55 \pm 0.08$. Again, the relatively large standard deviation results from the resolution of the Bourdon gages. This value compares well with the value $K_L^{cl} = 0.79$ computed from the data of Spears (undated, 27).

The pressure drop across the flow meter as a function of flow rate is given in the technical specifications for the device (Omega Engineering 2009). These data have been found to fit an equation of the form

$$\Delta P_{fm} = 0.251\dot{V}^2 + 0.006\dot{V} \quad (26)$$

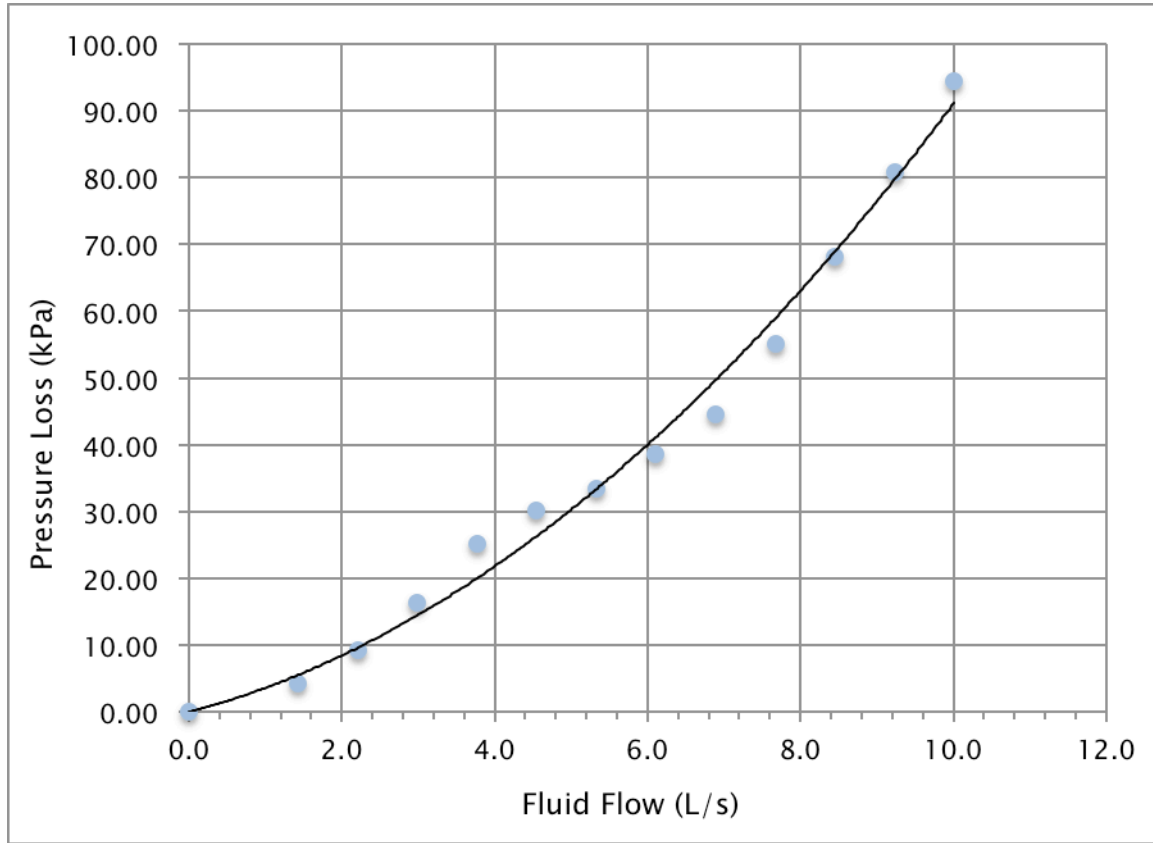


Figure 20: Pressure drop across the heat exchanger. The line is the least squares fit to the data, the equation for which is given in [Appendix 3](#).

where the pressure drop is given in kPa and the flow rate is in L/s. $R^2=1.000$ for this fit. At the flow rates under consideration here, the linear term is negligible. Solving Eq. (23) for the loss factor, we find that $K_L^{fm} = 1.725 \pm 0.003$, and is independent of the flow rate.

Finally, the loss factor for the heat exchanger may be determined. Since there are 3.48 m of CPVC pipe in the section between gages P1 and P2, the pressure drop across the CPVC pipe between P1 and P2 is

$$\Delta P_{CPVC/1-2} = 3.48 \Delta P_{CPVC/m} \quad (27)$$

and the pressure drop across the heat exchanger is

$$\Delta P_{he} = P1 - (P2 + \Delta P_{CPVC/1-2} + \Delta P_{fm}) \quad (28)$$

and is shown in Figure 20. As above, the loss factor is computed by inserting the data of Figure 20 into Eq. (23). In this case, the loss factor for the heat exchanger is strongly

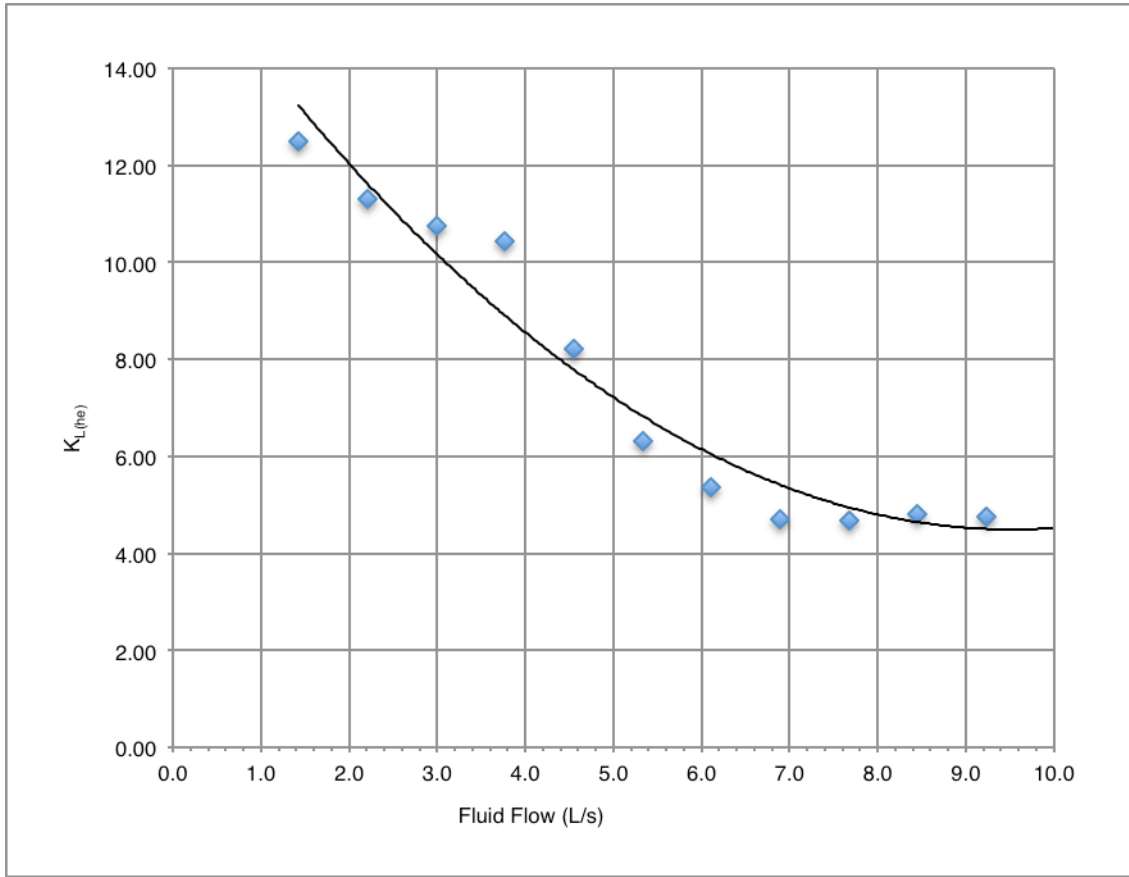


Figure 21: The loss factor of the heat exchanger, K_L , as a function of flow rate. The line is the least squares fit to the data, the equation for which is given in [Appendix 3](#).

dependent on the flow rate as illustrated in Figure 21 and is given by

$$K_L^{hc} = 0.134\dot{V}^2 - 2.544\dot{V} + 18.319 \quad (29)$$

where all variables have been previously defined. For these data, $R^2 = 0.953$.

As expected, the heat exchanger optimizes the amount of heat transfer in a fixed length through a geometrical design that increases both the heat sink surface area, as well as the overall surface dwell time through redirection of the flow in a helical pattern. The nature of this complex geometry affects the flow non-linearly, as illustrated by the large loss factor and its flow dependency as shown in Figure 21.

Operation of the system requires that the head pressure at the pump be less than the value specified by the pump specifications. The head at the pump outlet must include the

0.305 m difference between the height of the loop and the height of the fluid in the recirculating tank (Badr and Ahmed 2015, 21). This is given by

$$\Delta P_{hd} = 2.98 \text{ kPa} \quad (30)$$

where the pressure is given in kPa and is the equivalent to a pressure of 0.3 m of water at 4 °C. This quantity is so small compared to other effects that correction for the change in density of the fluid with temperature has been ignored.

Finally, the total length of CPVC pipe in the entire system is 11.43 m. This includes 1.22 m of CPVC pipe from the pump to P1, 3.48 m between P1 and P2, 0.46 m of pipe between P2 and P3, 4.60 m between P3 and P4, and another 0.91 m between P4 and the recirculating tank.

The total pressure drop in the system is thus

$$\Delta P_{loop} = \frac{1}{2} \left(11.43 K_L^{CPVC/m} + 4K_L^{ell} + K_L^{tm} + K_L^{hc} \right) \rho \dot{v}^2 \quad (31)$$

In deriving Eq.(31), frictional forces have been ignored in applying the Bernoulli equation. These effects are estimated to be only a few percent (Panton 2013, 132). The total pressure drop has been evaluated as a function of the fluid flow rate by using the least squares fits to the various components as listed in Appendix 3 and is shown in Figure 22.

Self-consistency requires that the pressure drop in the horizontal part of the loop be $\Delta P_{loop} = P_1$. A least squares plot of ΔP_{loop} calculated from Eq.(31) versus the values of P_1 calculated from the least squares values fit to the observed data of Figure 19 (see Appendix 3 for equations) shows that $\Delta P_{loop} = 0.983 P_1$ with $R^2 = 0.992$, thus confirming expectation.

The pump curve, obtained from the ASP technical specifications, is also shown in Figure 22 (American Stainless Pumps 2012).⁴⁴ The difference between the pump curve and the total pressure in the system describes the flow rate space that is available to the experimentalist in designing various sample configurations to be examined in the apparatus—the maximum

⁴⁴ We are indebted to Luke Eck of ASP for providing the head versus capacity data from the technical specifications in digital format.

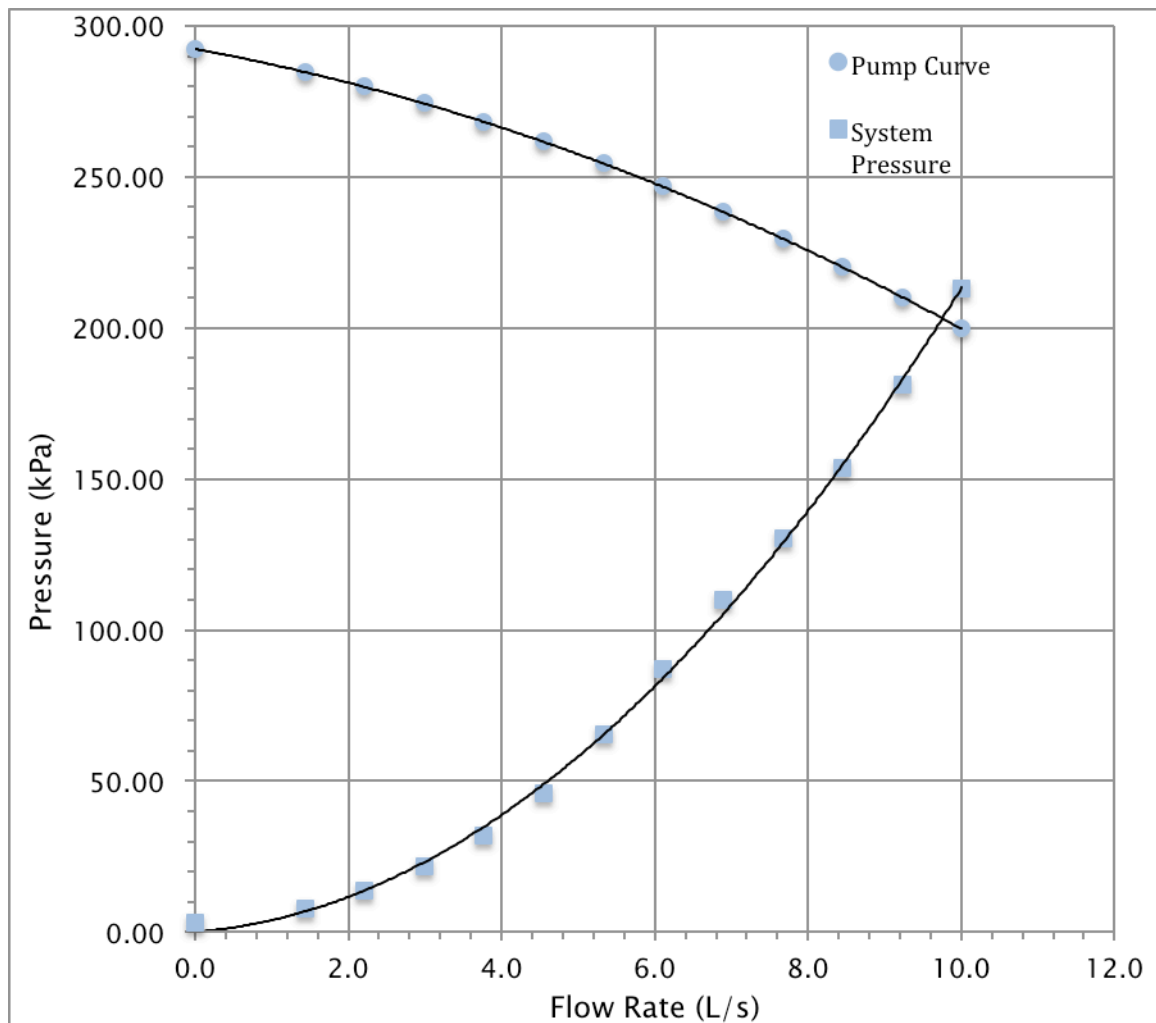


Figure 22: Pump curve and total system pressure. Solid lines are the least squares fit to the data and are given in [Appendix 3](#). The intersection of the two curves is the operating point of the system.

flow rate that can be accommodated is the operating point, the point where the two curves intersect.

These results show that the maximum flow rate through the system for any arbitrary experimental configuration is easily determined by adding the loss factor for the experimental apparatus to Eq.(31) and solving for the pressure and flow rate for which Eq. (31) and the pump curve intersect. In our laboratory, where we are interested in the effects of flow straighteners, valves, and orifices on the downstream corrosion and erosion of various alloys and on the surface treatments of pipes, such calculations are always

performed in advance of building and mounting the experiment in order to assure its feasibility. As noted in a previous section, we have developed a differential pressure system for measuring the loss factors of our experimental devices.

Experiment Loss Factors

The decrease in volumetric flow rate as a function of increasing loss coefficient as demonstrated in Figure 15 has significant implications for characterizing the fluid flow in any tribocorrosion study undertaken in the VTHTCL. In this section we develop an empirical relationship between flow rate and the loss coefficient.

Before beginning, it is essential to clarify terminology found in the literature. The loss factor, K_L , is a dimensionless quantity defined by Eq. (23) in the previous section, and the flow factor, K_v , is a dimensioned quantity defined by the Hazen–Williams equation (see Eq. (35) below). The latter is used to define the maximum flow rate through a valve as well as to define losses in other devices. In this section it will be necessary to use both terminologies. Relationships between the two are developed in Appendix 4.

The fluid flow effects of an experiment with a given loss coefficient may be studied by using the full-bore ball valve installed just before pressure gage P4 a proxy for the experiment by adjusting its closing angle, α . Examination of the loop diagram (Figure 1) shows that the following system of equations describes the pressure drop around the loop

$$\begin{aligned}
 P1-P2 &= \frac{1}{2} \rho \left(K_L^{he} + K_L^{fm} + l_1 K_L^{CPVC/m} \right) v^2 \\
 P2-P3 &= \frac{1}{2} \rho \left(2K_L^{el} + l_2 K_L^{CPVC/m} \right) v^2 \\
 P3-P4 &= \frac{1}{2} \rho \left(l_3 K_L^{CPVC/m} \right) v^2 + \Delta P_\alpha^{bv} \\
 P4-0 &= \frac{1}{2} \rho \left(l_4 K_L^{tube/m} \right) v^2 + \rho gh
 \end{aligned} \tag{32}$$

where ρ is the density of the fluid (kg/m³), the various K_L are the loss factors for the heat exchanger (he), the flow meter (fm), the CPVC pipe per unit length (m⁻¹), and other plumbing fixtures that make up the loop. The lengths $l_1 \dots l_4$ are the lengths of CPVC pipe (m) between the various pressure transducers, v is the mean velocity of the fluid (m/s), ΔP_α^{bv} is the pressure drop across the ball valve at an closing angle α , and h is the height of the exit tube (m) used to create sufficient backpressure to assure that at any flow rate the tube is always full. The pressures are given in pascals. The exit tube drains by gravity from

a height h into the recirculating tank, thus making the gage pressure at the exit zero. The small head from the recirculating tank to the entrance of the loop at $P1$ has been neglected as have the loss factors for the fully-open ball valves. Summing the four terms, the pressure drop from $P1$ around the loop to the recirculating tank is

$$P1 = \frac{1}{2} \rho K_L^{sys} v^2 + \rho g h + \Delta P_\alpha^{bv} \quad (33)$$

where the system loss factor is

$$K_L^{sys} = K_L^{he} + K_L^{fm} + (l_1 + l_2 + l_3) K_L^{PVC/m} + 2K_L^{el} + l_4 K_L^{PVC/m} \quad (34)$$

The pressure drop across the valve is given by the Hazen-Williams equation (Williams and Hazen 1914)

$$\Delta P_\alpha^{bv} = \frac{v^2 s}{\left(K_{v,SI}^\alpha\right)^2} \quad (35)$$

where s is the specific gravity of the fluid (dimensionless) and $K_{v,SI}^\alpha$ is the flow factor in the International System (SI) of units $\left(m/s\sqrt{kPa}\right)$.⁴⁵ Substitution of Eq.(35) in Eq.(33) and writing all pressures in pascals, the final expression for the pressure at $P1$ is

$$P1_\alpha = \frac{1}{2} \rho K_L^{sys} v^2 + \rho g h + \frac{v^2 s}{\left(K_{v,SI}^\alpha\right)^2} \quad (36)$$

If the value of the pressure for a fully open valve is taken as reference and subtracted from the pressure for a valve with a closing angle α ,

$$\Delta P^\alpha \equiv P1_\alpha - P1_0 = \left[\frac{1}{\left(K_{v,SI}^\alpha\right)^2} - \frac{1}{\left(K_{v,SI}^0\right)^2} \right] s v^2 \quad (37)$$

Eq.(37) is thus an expression for the pressure drop exclusively across the ball valve with a given closing angle, α , and can be determined from the experimental data of Figure 15. By

⁴⁵ We note that the units used in Eq.(35) are not the units commonly used in industry. The relationship between the industrial SI units and those used here is given in Appendix 5.

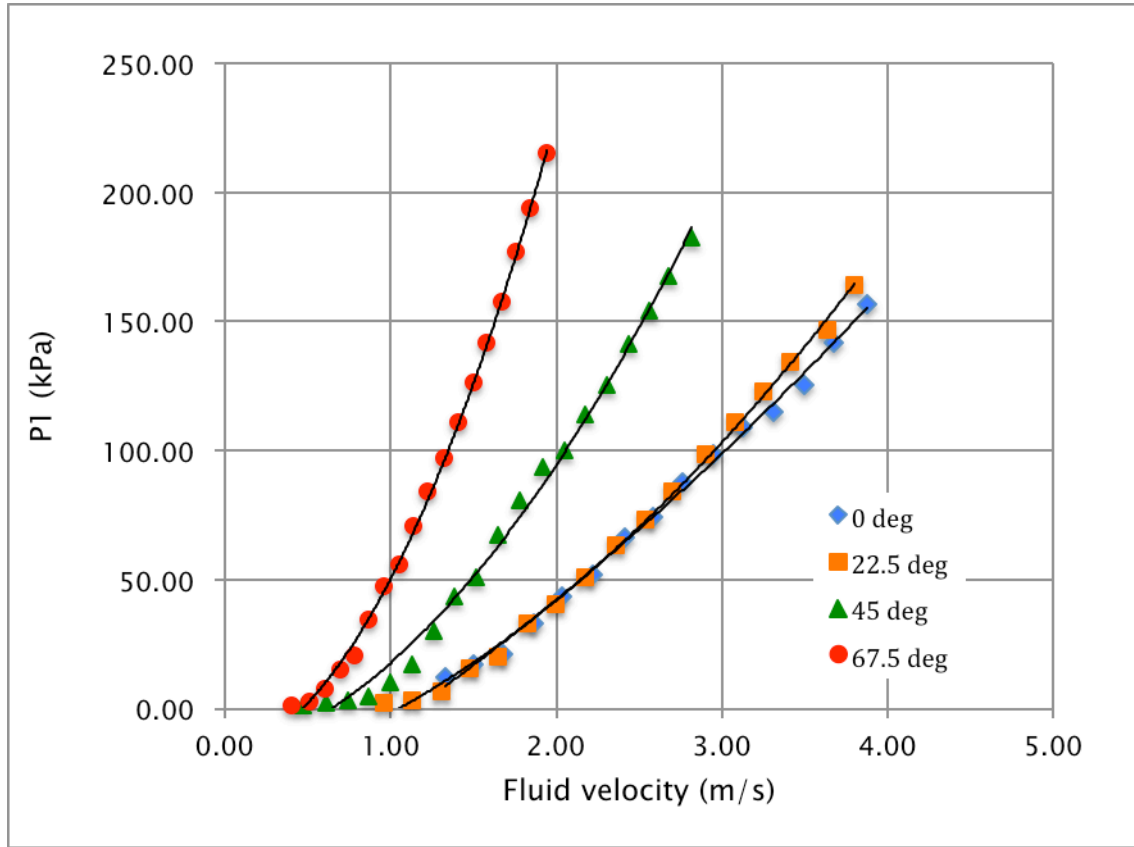


Figure 23: Pressure at P1 versus flow velocity as a function of the closing angle of a CPVC full-bore ball valve located just in front of pressure gage P4 in the VTHTCL. The least squares fits to the curves are given in [Appendix 3](#).

Eqs.(36) and (37) we expect that if the head pressure of the return loop is small, a graph of $P1^a$ versus the mean flow velocity should vary quadratically. That this is the case is shown in Figure 23. The pressure drop across the valve as expressed in Eq. (37) is presented in Figure 24. In this plot, the change in pressure was calculated at the various flow velocities by subtracting pressures computed from the least squares fits to the data in Figure 23. The predicted quadratic relationship between the pressure drop with flow velocity is confirmed for both the closing angles of 45° and 67.5°. The flow through, and hence the small pressure drop across, the valve at 22.5° is such that the relationship is not well obeyed as seen in Figure 24.

Let us define the variables (a_1, a_2, a_3) as

$$\begin{aligned}
a_1 &= \frac{s}{(K_v^{\alpha 1})^2} - \frac{s}{(K_v^{\alpha 0})^2} \\
a_2 &= \frac{s}{(K_v^{\alpha 2})^2} - \frac{s}{(K_v^{\alpha 0})^2} \\
a_3 &= \frac{s}{(K_v^{\alpha 3})^2} - \frac{s}{(K_v^{\alpha 0})^2}
\end{aligned} \tag{38}$$

From the data in Figure 24, the coefficients of the power law for the pressure given in Appendix 3 yield $(a_1=0.4859; a_2=12.555; a_3=40.453)$ where the subscripts (1,2,3) correspond to the valve closing angles 22.5, 45.0 and 67.5 degrees. Eqs.(38) are three equations in four unknowns. In order to determine the flow factors from these data, it is necessary to know the flow factor for a fully open valve. From Eq.(35), it is seen that if the fully open valve is frictionless, the flow factor must be infinite in order that there be no pressure drop across it. As an approximation, let us assume $K_{v,SI}^{\alpha=0}=\infty$. With this assumption, and taking the specific gravity of 3.5 weight percent salt water to be 1.025, the values of the flow factors at the other opening angles are readily found to be

$$\begin{aligned}
K_{v,SI}^{\alpha=22.5} &= 1.452(m/s\sqrt{kPa}) \\
K_{v,SI}^{\alpha=45.0} &= 0.286(m/s\sqrt{kPa}) \\
K_{v,SI}^{\alpha=67.5} &= 0.159(m/s\sqrt{kPa})
\end{aligned} \tag{39}$$

From the least squares fit to the experimental data, it is seen that the extrapolated flow factor for a fully open valve is expected to be $5.01(m/s\sqrt{kPa})$. Substitution of these values into Eq. (38) allows a second iteration of the flow factor values. However, such an iteration shows that, to the accuracy of the experimental results, the original hypothesis is valid. The values of the flow factors are compared with those from the literature in Figure 25. The results from the present experiment are approximately 47% of those given in MyDataBook (2018).

The loss coefficient, K_L , is defined by the equation (Munson et al. 2013, 415)

$$\Delta P = \frac{1}{2} \rho K_L v^2 \tag{40}$$

where, in SI units, the pressure drop across an assembly of pipes and fittings is given in pascals, the density of the fluid, ρ in kg/m³, and the fluid velocity in m/s. The loss

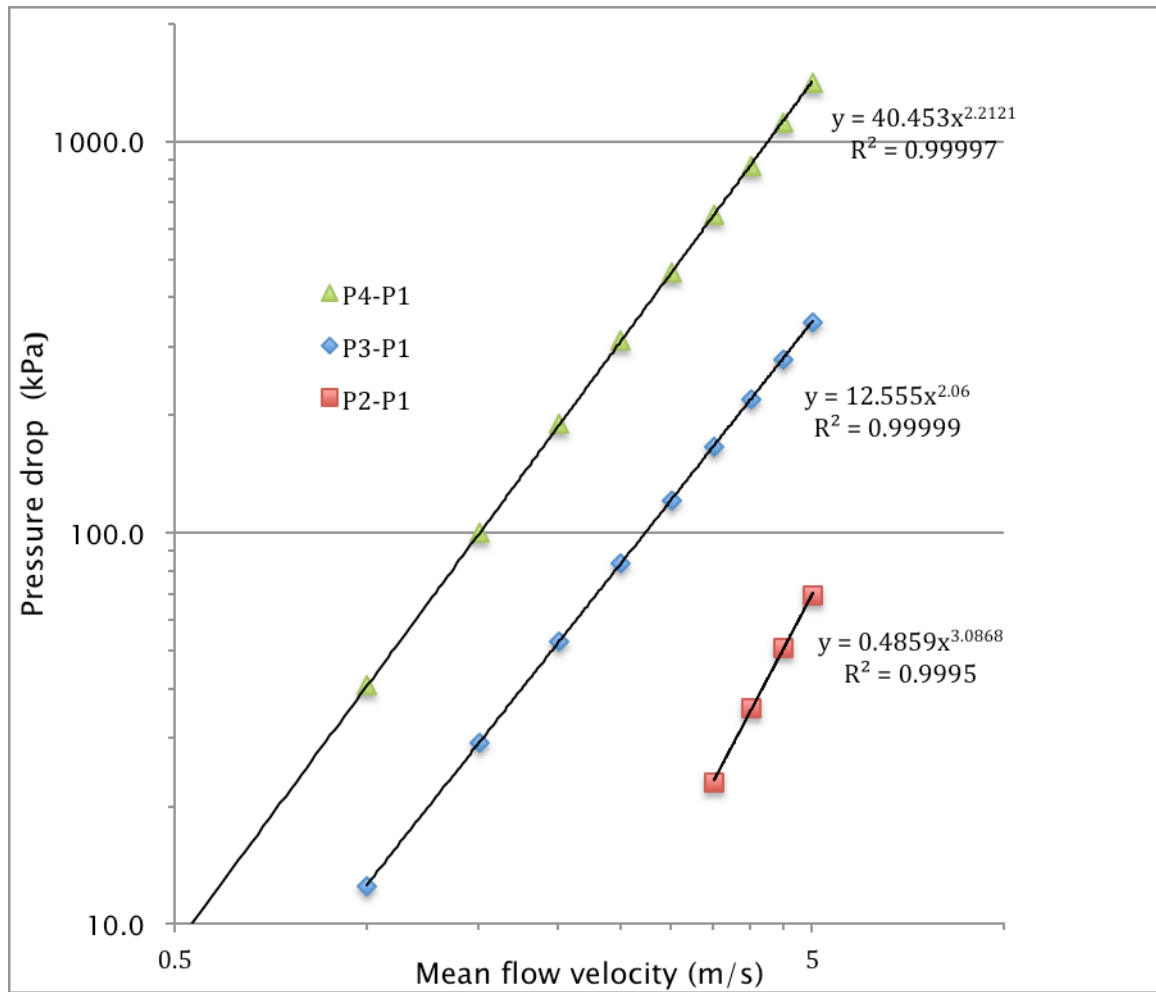


Figure 24: Pressure difference (kPa) across a CPVC full-bore ball valve as a function of mean flow velocity through the valve at three different opening angles. The least squares fits to the data are given in [Appendix 3](#).

coefficient is dimensionless. The quantitative relationship between the loss coefficient and the flow factor is developed in Appendix 4. The loss coefficients for the ball valve under consideration have been computed from the flow factor data shown in Figure 25 and are summarized in Table 2. The conversion from the SI units for the flow factor used in this paper and the industry standard (SU) units is also presented.

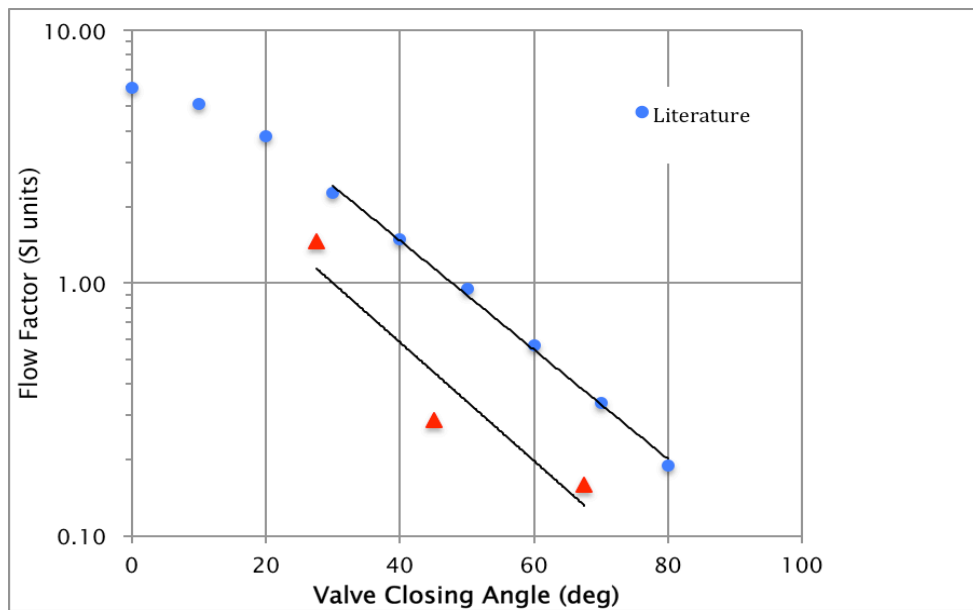


Figure 25: Flow factors, K_v for a full bore CPVC ball valve (SI units). The least squares fits to the data are given in [Appendix 3](#).

Table 2: Summary of experimental results for the loss coefficient and flow factors for a full bore ball valve as determined by pressure loss measurements in the VTHTVL. The flow factors are given in both Standard Units (SU) and in SI Units (SI) as discussed in the [Appendix 4](#).

Valve closing angle (degrees)	K_L	K_v (SI)	K_v (SU)
0.0	0.1	5.01	344.4
22.5	0.9	1.45	99.8
45.0	24.5	0.29	19.6
67.5	79.0	0.16	10.9

Effect of Backpressure (reprise)

Examination of Figure 15 shows that the volumetric flow rate depends linearly on the pump motor frequency and that the slopes of the curves are related to the loss factors of the valve. Since the valve is in the location of typical experimental apparatuses, the loss factors of the valve are proxies for the loss factors of experiments. The flow rate must be given by an expression of the form $\dot{V} = f \cdot g(K_L^\alpha)$ where f is the motor frequency (Hz). The function $g(K_L^\alpha)$ may be found by plotting a graph of slopes of the curves in Figure 15 versus the loss factors for the curves as is shown in Figure 26. From these results, the volumetric flow rate may be written as

$$\dot{V} = 0.1327(f - 0.15)e^{-0.0085K_L} \quad (41)$$

In Eq.(41) there is a small correction to the frequency to account for initial start-up of the pump. This correction is the average of the values for the four different curves as found in the least squares fits in Appendix 3. This equation fits the observed data to better than 3% for P1, P2, and P4 and better than 8% for P3.

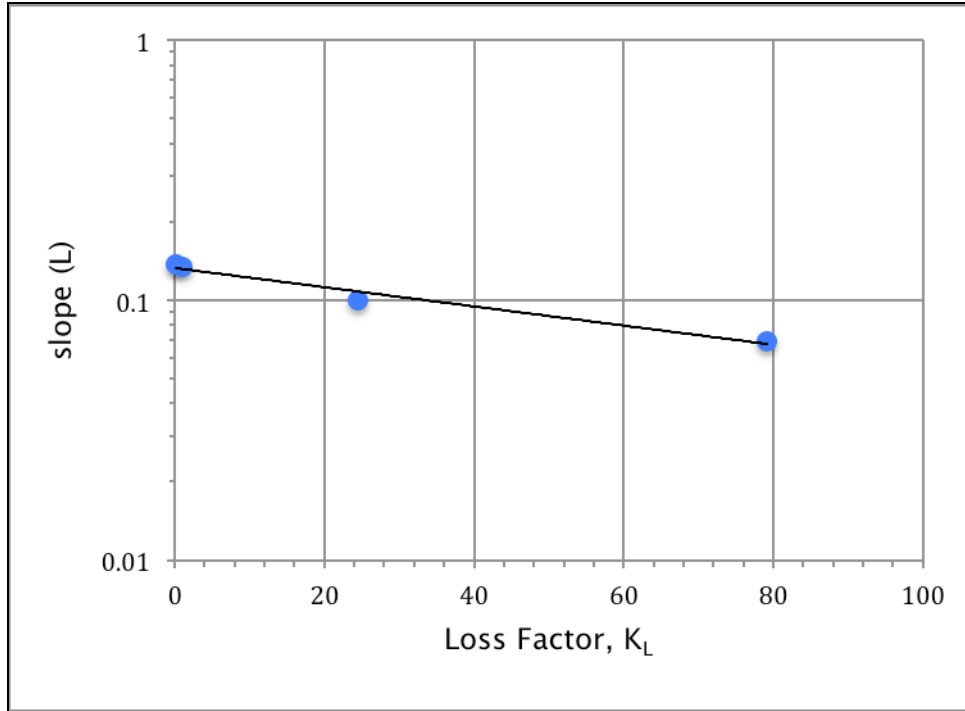


Figure 26: Semi-logarithmic plot of the slopes of Figure 15 versus the valve loss factor, K_L . The equation of the least squares fit to the data is given in [Appendix 3](#).

Gas Regulation

The three gases of interest for work in this laboratory are oxygen, nitrogen and argon. Oxygen (O₂) is available both as an injected high purity gas and as a component of ambient air, nitrogen (N₂) is available as a component of both injected compressed air and of ambient air, and argon (Ar) is available as an injected high purity gas. The delivery systems for all three gasses allow for each to be either bubbled through a small stainless steel tube at any level in the fluid or to be blown over the surface of the recirculating fluid in the surge tank.

The solubilities of Ar, N₂ and O₂ in both pure water and in seawater have been summarized in three IUPAC reports (Clever 1980; Battino 1981, 1982). Each is described by an equation of the form:

$$\ln(X_i) = A + B/(T/100) + C \ln(T/100) + D(T/100) \quad (42)$$

where X_i is the mole fraction solubility at 1.0 atm (101.325 kPa) of the i^{th} component and T is the temperature in K. The constants A, B and C for the three gasses, as taken from these references, are given in Table 3 and their solubilities as a function of temperature at 1 atm. of pure gas are shown in Figure 27. We note that the calculated values for the solubility of Ar in water using only the first three values given in Table 3 are significantly higher than those presented in Table 1 of (Clever 1980). This inconsistency appears to be caused by the omission of the linear term in Eq. (42) of the form $D*(T/100)$. We have estimated that the missing term is $D=-0.2885$. The data shown in Figure 27 have been corrected for this omission.

The solubility of each gas is, by Henry's Law, the value shown in Figure 27 multiplied by the partial pressure of the gas. Since the recirculating tank is open to atmospheric pressure, the sum of the partial pressures of all three gasses must be the local atmospheric pressure, or

$$p_A + p_{N_2} + p_{O_2} = P_{\text{atm}} \quad (43)$$

where $p_A + p_{N_2} + p_{O_2}$ are the partial pressures of argon, nitrogen, and oxygen, respectively. Thus, for operation of the loop at any given temperature, the concentration of dissolved oxygen can be controlled by controlling its partial pressure by adjusting the argon in the space above the recirculating fluid in the recirculating tank.

Table 3: Water Solubility Constants for Eq. (42).

Gas	A	B	C	D	Ref
Ar	-57.6661	+74.7627	+20.9318	-0.2885	(Clever 1980)
N ₂	-67.3877	+86.3213	+24.7891	0.	(Battino 1982)
O ₂	-66.7354	+87.4755	+24.4526	0.	(Battino 1981)

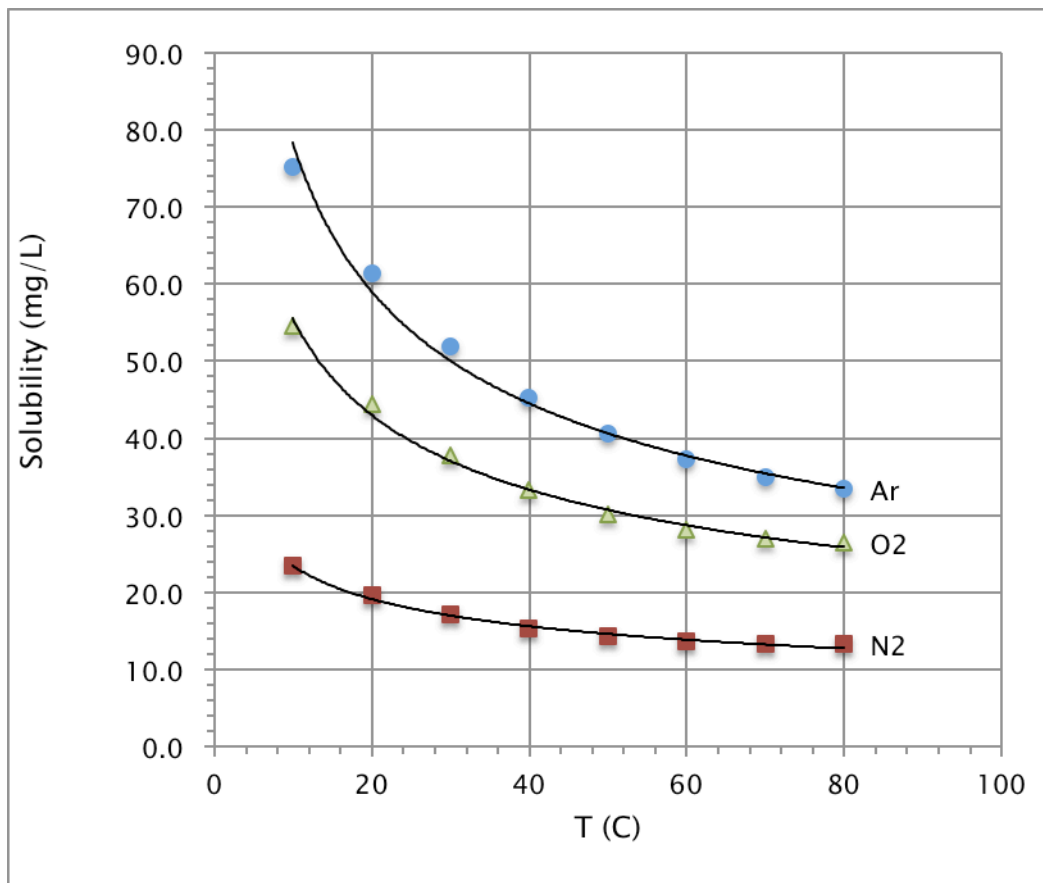


Figure 27: Solubility of argon, nitrogen and oxygen in water versus temperature. Each curve is for 1 atm. of pure gas over the solvent. The lines are given by Eq. (42) using the values of Table 3.

Table 4: Dissolved oxygen (DO_{obs} =measured value) versus the equilibrium concentration as a function of temperature.

T (C)	DO_{obs}	DO_{eq}	ratio
22.8	4.9	8.6	0.57
28.8	3.1	7.8	0.40
61.1	7.2	5.7	1.27

As a test of this concept, the system was filled with distilled water and run at various flow rates from 1.39 to 5.93 L/s with the heat exchanger operating its full capacity of 0.60 L/s. Argon was flowed through the system at 40 ccm and bubbled from the bottom of the recirculating tank. Under these conditions, the average temperature of the system was 12.6 ± 0.9 C at which the equilibrium concentration of dissolved oxygen under 1 atmosphere of air is 10.5 ± 0.3 mg/L. The measured concentration of oxygen under the Ar atmosphere was 3.9 ± 0.2 mg/L, a reduction to 37% of the equilibrium concentration.

The identical experiment was run under the conditions of no chilled water flow in the heat exchanger. Here, the system was allowed to run for several hours until the temperature in the recirculating tank equilibrated (See Figure 18). The results of this experiment are shown in Table 4. Here, it is seen that, except for the highest temperature, the dissolved oxygen is also reduced below the equilibrium concentration, but that there is more uncertainty in the data than at the lower temperatures. The excess oxygen at the highest temperature needs further study.

Scalability

While the aforementioned apparatus and its capabilities have been designed and developed around commercially available two-inch pipe, the relevance and significance of this apparatus relies upon the scalability of the data. In the case of corrosion and erosion studies, the parameters of interest are the wall shear stress and the thickness of the surface boundary layer. Thus, it is critical to understand how these parameters scale with the size of the pipe or tubing under investigation. We have independently performed calculations based upon generally accepted concepts of turbulent flow of incompressible fluids and have verified our results with computational fluid dynamics (CFD) (Munson et al. 2013; Panton 2013). This work suggests an expected power law relationship between the thickness of the laminar sub-layer and the wall shear that is independent of pipe size. As

well, a linear relationship is expected between a modified Euler number, a ratio of the shear force over inertial force $\left(\tau/\rho\dot{v}^2\right)$, and the friction factor that is also independent of pipe size. Thus, the kinetics of growth of protective oxide layers should not be expected to scale linearly with the Reynolds number of the fluid flow, but an appropriately more complex scaling has been identified. Experimental research is underway to verify these anticipated relationships.

Conclusions

The Virginia Tech high turbulence corrosion loop (VTHTCL) is a unique new instrument that has been developed for the study of corrosion, erosion and tribocorrosion of metal samples under highly turbulent conditions during which the flow, the fluid chemistry and the corrosion/ erosion of the material under investigation may be quantitatively monitored. This system features:

- ❖ Turbulent flow rates of aqueous solutions from approximately 0.32 L/s to 9.46 L/s through a 51 mm pipe over a temperature range from 11 °C to 80 °C. The nominal Reynolds number of the maximum flow rate is 295,000 at RT and approximately 800,000 at 80 °C.
- ❖ Laminar flow rates in the range $200 \leq Re \leq 1200$ using a small auxiliary pump.
- ❖ A gas handling system that allows for the control of dissolved oxygen in the fluid at levels below those of the equilibrium concentration of oxygen in the normal atmosphere.
- ❖ Instrumentation to quantitatively monitor the fluid flow rate, temperature, pressure, pH, dissolved oxygen, and conductivity via a computer data acquisition system.
- ❖ Insertion bays for easy exchange of experimental configurations, thus allowing several investigators to develop specimen chambers off line and mount them as time becomes available in the loop.
- ❖ A safety system that shuts the system down in case of a loss-of-fluid or a thermal runaway accident and that has shields to protect personnel in the event of a burst line filled with scalding water.
- ❖ A suite of general-purpose sample chambers that allow the insertion of a wide variety of devices for simulating valves and flow straighteners into the loop.

Experimental data and computations quantify and demonstrate several operating conditions, including:

- ❖ The heating of the fluid due to the high turbulence of the fluid and the performance of the heat exchanger in mitigating this heating.
- ❖ The temperature of the fluid at any point in the system intermediate between the locations of thermocouples.
- ❖ The effects of the pressure drop across various components, including the heat exchanger, the flow meter, and the piping system on the operating capabilities of the machine and on the constraints they impose on the design of experiments.
- ❖ The measures of the flow factors and the loss coefficients of various components that agree acceptably with the literature.
- ❖ The development of a quantitative expression that gives the volumetric flow rate of the fluid as a function of both the pump motor frequency and the loss coefficient of the experimental apparatus.
- ❖ The capability of using an argon gas cover that allows the dissolved oxygen to be reduced by as much as a factor of three below the equilibrium concentration under normal atmospheric conditions.

Acknowledgements

This research was supported in part by a grant from the US Department of Energy, Office of Nuclear Energy, Scientific Infrastructure Award (Award#: DE-NE0008674; Project #: GSI-17-13340), in part by the Naval Surface Warfare Center-Carderock Division through a Cooperative Research and Development Agreement (NCRADA-NSWCCA-17-279) between our organizations, and by the Materials Science and Engineering Department at Virginia Tech.

The instrument described here is the result of the efforts of three undergraduate Senior Design teams spread over three consecutive academic years as well as independent research by three other undergraduates and by the graduate research of three students. Erik Cothron, Ryan Taylor and Peter Todoroff undertook the design and development of the first iteration of the instrument as their Senior Project in AY 2015/2016. As a result of the successes of the initial incarnation, each chose to continue his education as an MSc student and continued their work on the instrument. John Lones, Trent Strickland, Trey Vanhout, and Joel Zilke reconstructed the original 5 m long loop as the current 10 m loop, installed

the heat exchanger, and developed the first LabView control program during the 2016/2017 AY, while Justin Aird, Alison Carney, Dustin Rose and Will Wenger added more instrumentation to improve the measurement and control of the fluid chemistry, made significant improvements to the instrumentation wiring, added the capabilities to monitor the wall thickness of the sample tubes via ultrasonic techniques, and made several advancements in the LabView control code during the 2017/2018 AY. Ben Greenblatt, Trey Vanhout and Will Wenger each made significant contributions to the calibration of the fluid flow (Ben), characterizing the heat exchanger (Trey), and developing mechanical components of the instrument (Will). As graduate students Peter, Ryan and Erik provided their expertise and guidance to the incoming undergraduates in all aspects of the design, improvement, and operation of the instrument.

An effort of this magnitude could not have been accomplished without the help of numerous people and corporations. We wish to thank: Dr. Elissa Trueman of the Naval Surface Warfare Center – Carderock Division for valuable discussions of corrosion under high turbulence; Luke Eck of American Stainless Pumps, Inc. for assistance in selecting the correct pump and motor system; Sam Mirza of Hitachi Industrial Equipment Systems, Co. Ltd. for assistance with the selection and installation of the variable frequency drive; Tim Ayres and Jason Lawe of Fluid Chillers for the design and implementation of the heat exchanger, and Eden Klingenberg, Matt Pegram, and Kira Theuer of National Instruments for assistance with the LabVIEW programming language. We would also like to give special thanks to Dr. Tony Trueman for his valued guidance in the field of corrosion and electrochemistry.






Various staff and faculty from the Virginia Tech university community provided invaluable technical support: Jim McDaniel was the project manager for the installation of the power systems and Joe Zokaite, the University Building Official, helped assure the safe design and installation of the power control panels; James Lambert of the AOE machine shop supervised the precision machining of the control panels, safety shields and the universal sample chamber; Dr. Carlos Suchicital, Hesham Elmkharram, and Ibrahim Khalfallah of the MSE facilities group were invaluable with their help in assembly of the system. Professor Joseph Schetz provided valuable discussion concerning turbulent fluid flow in the system and Profs. Thomas Staley, Sean Corcoran and Alan Druschitz assisted with a myriad of issues associated with thermodynamics, fluid flow, and corrosion. Ms. LeeAnn Ellis provided assistance with the photographs of the various components of the system. Finally, we thank Prof. David Clark, Department Head and the MSE Department for financial support.

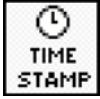



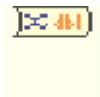

Appendices





Appendix 1: Compact DAQ Chassis (cDAQ-9188) Modules

Module Slot	Module (Model #)	Description	Sensors/Actuators
1	Thermocouple Input (NI-9213)	16-Channel, 75 S/s thermocouple module	Heat Exchanger 1. Fluid Inlet 2. Fluid Outlet 3. Coolant Inlet 4. Coolant Outlet
2	Relay Output (NI-9482)	4-Channel, 5Vdc electromechanical switch relay module	1. Switch to analog relay
3	Voltage Input (NI-9201)	8-Channel, ± 10 V, 500 kS/s voltmeter module	1. Heat Exchanger Valve Actuation 2. 54W Auxiliary Pump 3. 5V Safety Check
4	Bridge Input (NI-9237)	4-Channel, 50 kS/s strain gage bridge module	1. Wall Shear Sensor
5	Current Input (NI-9203)	8-Channel, ± 20 mA, 200 kS/s current meter module	1. Flow Meter 2. Dissolved Oxygen Meter 3. pH (upstream) Meter 4. pH (downstream) Meter 5. Conductivity (upstream) Meter 6. Conductivity (downstream) Meter 7. Metal Samples® LPR Data Logger 8. Metal Samples® ER Data Logger
6	Current Input (NI-9203)	8-Channel, ± 20 mA, 200 kS/s current meter module	1. Pressure Gage P1 2. Pressure Gage P3 3. Pressure Gage P4 4. Differential Pressure Gage 5. ---- 6. ----
7	Current Input (NI-9203)	8-Channel, ± 20 mA, 200 kS/s current meter module	Reserved for parallel tube assembly
8	Reserved		

Appendix 2: AMS Subroutine Descriptions

Category Subroutine Name (Origin)	Icon	Level, Purpose & Description
Email Send SMTP (Author)		Level II: SMTP procedures to connect to a specified email server with stored credentials, compose message with attached files, and send
String SMTP Subject (Author)		Level II: Concatenates entered strings into a single string for the subject line of an email
String User & Experiment Information (Author)		Level II: Concatenates entered experimental information (as string form) into a single string for the body of an email
String 20% Environmental Conditions Differential (Author)		Level II: Performs “Within Range” for select environmental conditions to indicate a greater than $\pm 20\%$ from the previous reading. Compiles the names of each individual condition that exceeds and concatenates into a single string.
DAQ UT Multiple Transducers (Author)		Level II: Performs “UT Measurement – Single Transducer” for a specified quantity of UT transducers. Compiles individual channels into a 1D array, multiple channel dynamic data form

String Time Stamp (Author)		Level II: Generates a time stamp from the computer's system time in 1D array, multiple channel dynamic data form
DAQ NI Module Measurements (Author)		Level II: Returns the RMS (Statistics) of selected module channels from the NI chassis (DAQ Assistant) for 5 samples at 5Hz. Writes attributes to each channel, and converts the data into appropriate units from, takes the average of similar data groups, and converts into dynamic data form (to dynamic data).
Write to Measurement File (Internal)		Level II: Writes all multiple channel, dynamic data to a single, user named spreadsheet file. Newly acquired data is appended to the same spreadsheet each iteration the subroutine is executed.
Analysis 20% Environmental Conditions Differential (Author)		Level III: Gives a Boolean response if a current reading is within $\pm 20\%$ from the previous reading
Convert from Dynamic Data (Internal)		Level III: Converts the dynamic data type to numeric, Boolean, waveform, and array data types for use with other VIs and functions.
DAQ UT Single Transducer (Author)		Level III: Selects the designated UT multiplexer channel and transducer (A-O), transmits and queries serial commands to the UT instrument, writes the measurement command into 1D array, single channel dynamic data form

Convert to Dynamic Data (Internal)		Level III: Converts a Boolean, waveform, and or array data to several different types of data; single numeric value, single channel, multiple channels for waveforms or indicators (numeric or Boolean)
DAQ Assistant (Internal)		Level III: Creates, edits, and runs tasks using NI-DAQmx
Statistics (Internal)		Level III: Returns the selected parameter of the first signal in a waveform. For RMS, it performs for all signal values that enter.
Instrument I/O Assistant (Internal)		Level IV: Establishes a connection to an instrument via a physical communication port and allows a user to send serial commands.

Appendix 3: Least squares fit parameters to observed data.

Figure	Least squares Fit to the Data [‡]	R ²
Figure 14	$\dot{V} = 0.1516f - 0.1295$	1.000
Figure 15	For P1: $\dot{V} = 0.137f - 0.2015$	1.000
Figure 15	For P2: $\dot{V} = 0.1346f - 0.1999$	1.000
Figure 15	For P3: $\dot{V} = 0.0996f - 0.0946$	1.000
Figure 15	For P4: $\dot{V} = 0.0695f - 0.1026$	0.999
Figure 16	$\dot{V} = 0.0042V - 0.0050$	0.992
Figure 17	$\ln\left(\frac{T(t)-T_f}{T_i-T_f}\right) = 6.68 \times 10^{-3}t + 0.0138$	0.997
Figure 18	$\Delta T = 6.514 \times 10^{-3} f^{2.50}$	1.000
Figure 19	$P1 = 1.846\dot{V}^2 + 0.702\dot{V}$	0.981
Figure 19	$P2 = 0.793\dot{V}^2 - 2.282\dot{V}$	0.990
Figure 19	$P3 = 0.492\dot{V}^2 - 1.312\dot{V}$	0.989
Figure 19	$P4 = 0.337\dot{V}^2 - 2.157\dot{V}$	0.945
Figure 20	$\Delta P_{he} = 0.608\dot{V}^2 + 3.022\dot{V}$	0.990
Figure 21	$K_L^{h\nu} = 0.134\dot{V}^2 - 2.541\dot{V} + 18.319$	0.953
Figure 22	$\Delta P_{pump} = -0.458\dot{V}^2 - 4.657\dot{V} + 292.3$	1.000
Figure 22	$\Delta P_{loop} = 1.939\dot{V}^2 + 1.912\dot{V}$	0.999
Figure 23	$P1^{\alpha=0} = 4.080v^2 + 36.325v - 46.896$	0.997
Figure 23	$P1^{\alpha=22.5} = 8.716v^2 + 17.548v - 27.923$	0.998
Figure 23	$P1^{\alpha=45} = 19.679v^2 + 17.774v - 19.676$	0.994
Figure 23	$P1^{\alpha=67.5} = 55.084v^2 + 13.901v - 18.375$	0.999
Figure 24	$P2 - P1 = 0.486v^{3.09}$	1.000
Figure 24	$P3 - P1 = 12.555v^{2.06}$	1.000
Figure 24	$P4 - P1 = 40.453v^{2.21}$	1.000
Figure 25	$K_{v,sl}^{\alpha} = 10.736e^{-0.050\alpha}$ (lit)	0.997
Figure 25	$K_{v,sl}^{\alpha} = 5.010e^{-0.054\alpha}$ (exp)	0.890
Figure 26	$g(K_L) = 0.1327 \exp(-0.0085 K_L)$	0.973

[‡]Units are defined in the figures.

Appendix 4: Flow factors and Loss factors

The pressure drop across a valve is given by the Hazen–Williams equation (Williams and Hazen 1914)

$$\Delta P_{\alpha}^{bv} = \frac{\dot{Q}^2 s}{\left(K_{v,SU}^{\alpha}\right)^2} \quad (\text{A.1})$$

where, in the units commonly given in the literature, \dot{Q} is the flow rate (m^3/hr), s is the specific gravity of the fluid (dimensionless), and $K_{v,SU}^{\alpha}$ is the flow factor for the valve at an closing angle α and is given in units of $(\text{m}^3/\text{hr})/\sqrt{\text{bar}}$ where the pressure drop is given in bars. The subscript SU indicates that this value of the flow factor is given in “standard units” found in the literature (e.g., MyDatabook.org 2018). For use in Eq.(33), the units of the flow factor must be consistent with those of the remainder of the equation. Therefore, we define a value of the flow factor by the equation

$$\Delta P_{\alpha}^{bv} = \frac{v^2 s}{\left(K_{v,SI}^{\alpha}\right)^2} \quad (\text{A.2})$$

where $K_{v,SI}^{\alpha}$ is the flow factor in more traditional System International (SI) units $(\text{m}/\text{s}\sqrt{\text{kPa}})$. We choose to use the mean velocity of the fluid (in m/s) to describe the fluid flow and to express the pressure in kilopascals (kPa). The subscript SI is used to denote the flow factor in these units. Performing the coordinate transformation between the SU and SI units, we find

$$K_{v,SI}^{\alpha} = \left(\frac{4}{36000\pi D_i^2}\right) K_{v,SU}^{\alpha} \quad (\text{A.3})$$

where D_i is the internal diameter of the pipe/tube. Again, the subscripts SU and SI define the standard units of flow factors found in the literature (SU) and those that are used in this paper (SI). For Schedule 80 tubes, the ID is 0.0492 m and

$$K_{v,SI}^{\alpha} = 1.455 \times 10^{-2} K_{v,SU}^{\alpha} \quad (\text{A.4})$$

The loss factor across a ball valve is then found from the relationship

$$\Delta P^a = \frac{1}{2} \rho \frac{K_L^a}{1000} v^2 = \frac{sv^2}{(K_{v,SI}^a)^2} \quad (\text{A.5})$$

where the factor of 10^3 in the denominator of the middle term is to convert the pressure to kPa and the right-hand term is Eq.(A.2). Solving Eq.(A.5) for the loss coefficient, we find

$$K_L^a = \frac{2 \times 10^3 s}{\rho (K_{v,SI}^a)^2} = \frac{2 \times 10^3}{\rho_{H_2O} (K_{v,SI}^a)^2} \quad (\text{A.6})$$

The standard measurements are made at 16 °C at which temperature the density of water is 999.1 kg/m³, and thus

$$K_L^a = \frac{2.001}{(K_{v,SI}^a)^2} \quad (\text{A.7})$$

If the loss coefficient is to be computed from the flow factor given in standard units (SU), then the flow factor must be converted from SI to SU units as given by Eq. (A.4) and is

$$K_L^a = \frac{0.945 \times 10^4}{(K_{v,SU}^a)^2} \quad (\text{A.8})$$

Appendix 5: List of acronyms, alloy designations, and pipe sizes

Acronym	Definition
AA	The Aluminum Association
AISI	American Iron and Steel Institute
AMS	Apparatus monitoring system
ANSI	American National Standards Institute
CPVC	Chlorinated polyvinylchloride
CSV	Comma separated variable file
DUT	Device under test
ER	Electrical resistivity (type of corrosion sensor)
ESP	Emergency shutdown procedure
ISO	International Standards Organization
LPR	Linear polarization resistance (type of corrosion sensor)
PID	proportional–integral–differential (type of electronic controller)
PRT	Platinum resistance thermometer
PVC	Polyvinylchloride
SAE	Society of Automotive Engineers International
SCRAM	Shut down in an emergency (from nuclear reactor terminology)
SMTF	Simple mail transfer protocol (standard protocol for sending email across the internet)
UNS	Unified Numbering System (a system for identifying alloys)
UT	Ultrasonic transducer
VFD	Variable frequency drive
VHTCL	Virginia Tech high turbulence corrosion loop

Alloy Designations by Various Standards Organizations					
AA	AISI	ISO	SAE	UNS	References
AA2024–T3		2024–T3	A2024	A2024	(ANSI 1979; ISO 2007; Aluminum Assoc. 2015; ANSI 2017)
NA	304	X5CrNi18–9	304	S30400	(ANSI 1979; SAE 2017)
NA	316	X5CrNi17–12–3	316	S31600	(ANSI 1979; SAE 2017)

Nominal Dimensions for NPS 2-in (DN 50 mm) Pipe					
Schedule	Nominal Size	OD (mm/in)	ID (mm/in)	Wall	Reference
STD/40	50/2	60.33/2.375	52.51/2.067	3.912/0.154	(ANSI
XS/80	50/2	60.33/2.375	49.26/1.939	5.537/0.218	(ANSI

Appendix 6: List of Variables

List of Variables		
Variable	Definition	Units
A, B, C, D	Water solubility constants for gasses in water (Eq.(42))	--
ccm	Cubic centimetres per minute	cm ³ /min
C	Constant relating Grashof-Prandtl number to Nusselt number (Eq. (15))	--
C _p	Heat capacity at constant pressure	J/mol · K
D_i	Inner diameter of pipe	m
D_o	Outer diameter of pipe	m
f	Pump motor frequency	Hz
g	Gravitational constant (=9.81)	m/s ²
Gr	Grashof number (Eq. (14))	--
h _a	Heat transfer coefficient of air	W/m ² · K
k _a	Thermal conductivity of air (Eq. (16))	W/m · K
k _{CPVC}	Thermal conductivity of CPVC	W/m · K
$K_L^{CPVC/m}$	Loss factor for CPVC (per meter)	m ⁻¹
K_L^{elbow}	Loss factor for elbow	--
K_L^{fm}	Loss factor for flow meter	--
K_L^{he}	Loss factor for heat exchanger	--
$K_{V,SI}$	Flow coefficient	$\left(\frac{m}{s\sqrt{kPa}} \right)$
$K_{L,SU}$	Flow coefficient	$\left(\frac{m^3}{hr\sqrt{bar}} \right)$
L	Length of pipe	m
m	Mass of fluid	kg
m	Constant relating Grashof-Prandtl number to Nusselt number (Eq. (15))	--
Nu	Nusselt number (Eq. (15))	--
$p_A, p_{O_2}, \text{ and } p_{N_2}$	Partial pressures of argon, oxygen and nitrogen (Eq. (43))	kPa
P _{atm}	Atmospheric pressure	kPa
P1, P2, P3, and P4	Pressures at locations 1, 2, 3 and 4 in the line (Fig. 1)	kPa
Pr	Prandtl number (Eq. (14))	--
q	Heat loss	W/m
q'	Heat loss per unit length (Eq. (17))	W/m ²
q''	Heat loss per unit length (Eq. (18))	W/m ²
R _i	Inner radius of pipe	m

R_o	Outer radius of pipe	m
List of Variables (cont'd)		
Variable	Definition	Units
Re	Reynolds number	--
t	time	s
T	temperature	K; °C
T_a	Ambient temperature	°C
T_f	Equilibrium final temperature (Eq. (6))	°C
T_f	Film temperature (Eq. (14))	K
T_i	Equilibrium ignition temperature (Eq. (6))	°C
T_w	Wall temperature (Eq. (14))	K
T_∞	Ambient temperature (Eq. (14))	K
\dot{v}	Mean linear flow velocity in pipe	m/s
\dot{V}	Volumetric flow rate of fluid in pipe	L/s
X_i	Mole fraction solubility of i^{th} component of atmosphere (Eq. (42))	--
β	Inverse of absolute temperature (Eq.(14))	K ⁻¹
ΔP_{loop}	Pressure drop around the corrosion loop (Eq. (31))	kPa
$\Delta P_{CPVC/m}$	Pressure drop of CPVC per meter	kPa/m
ΔP_{fm}	Pressure drop across the flow meter	kPa
ΔP_{he}	Pressure drop across heat exchanger	kPa
ρ	Fluid density	kg/m ³
τ	System thermal time constant (Eq. (6))	s
ν	Kinematic viscosity of fluid (air or pumped fluid, as appropriate)	m ² /s

References

- AK Steel. 2013. Technical Report *316/316L Stainless Steel Product Data Bulletin*. West Chester, OH: AK Steel.
http://www.aksteel.com/pdf/markets_products/stainless/austenitic/316_316l_data_bulletin.pdf, accessed 27 May 2017.
- Aluminum Assoc. 2015. *International Designation and Chemical Composition Limits for Wrought Aluminum and Wrought Aluminum Alloys*. Arlington, VA: The Aluminum Association.
- American Stainless Pumps. 2012. Technical Report C24660–3500: *Technical Specifications, ASP 4.75" Diameter Impeller C24660 3500-rpm*. Los Angeles, CA: American Stainless Pumps. <http://www.asppumps.com/wp-content/uploads/C24660-3500.pdf>, accessed 4 Jun 2017.
- ANSI 1979. Standard B36.10–1979, in *American National Standard for Welded and Seamless Wrought Steel Pipe*. New York, NY: American National Standards Institute.
- ANSI 2017. Standard H35.1 /H35.1M2017, in *American National Standard Alloy and Temper Designation System for Aluminum*. New York, NY: American National Standards Institute. (Note: Revises AA ANSIIH35.1.)
- ASME 2001. Standard ASME MFC–8M–2001, in *Fluid Flow in Closed Conduits: Connections for Pressure Signal Transmissions Between Primary and Secondary Devices*. New York: American Society of Mechanical Engineers.
- ASME 2004. Standard MFC–3M–2004, in *Measurement of Fluid Flow in Pipes Using Orifice, Nozzle, and Venturi*. New York: American Society of Mechanical Engineers.
- ASME 2007. Standard MFC–3Ma–2007, in *Addenda to Measurement of Fluid Flow in Pipes Using Orifice, Nozzle, and Venturi*. New York: American Society of Mechanical Engineers.
- Badr, H. M., and W. H. Ahmed. 2015. *Pumping Machinery Theory and Practice* 1st ed. Hoboken, NJ: John Wiley and Sons.

- Battino, R., ed. 1981. IUPAC–NIST Solubility Data Series: Vol. 7, Oxygen and Ozone. A. S. Kertes, series ed. New York: Pergamon Press.
<https://srdata.nist.gov/solubility/index.aspx>, accessed 13 Jan 2018.
- Battino, R., ed. 1982. IUPAC–NIST Solubility Data Series: Vol. 10, Nitrogen and Air. A. S. Kertes, series ed. New York: Pergamon Press.
<https://srdata.nist.gov/solubility/index.aspx>, accessed 13 Jan 2018.
- Boedecker Plastics. "PVC (PolyVinyl Chloride) & CPVC (Chlorinated PolyVinyl Chloride) Specifications." Shiner, TX: Boedecker Plastics Accessed 22 May 2017.
http://www.boedecker.com/pvc_p.htm.
- Carney, A. A., and R. W. Hendricks. 2017. "The Viscosity of Dilute H₂O–B(OH)₃–LiOH Solutions." Corrosion 2017, New Orleans, LA, 26–30 Mar 2017.
- Clever, H. L., ed. 1980. IUPAC–NIST Solubility Data Series: Vol. 4, Argon. A. S. Kertes, series ed. New York: Pergamon Press. <https://srdata.nist.gov/solubility/index.aspx>, accessed 13 Jan 2018.
- Cothron, E. A., R. C. Taylor, and P. K. Todoroff. 2016. "An Apparatus for the Investigation of Turbulence on the Erosion–Corrosion of Piping Materials." Homework assignment for Senior Design, Materials Science and Engineering Department. Virginia Tech, Blacksburg, VA.
- Cothron, E. A., R. C. Taylor, P. K. Todoroff, and R. W. Hendricks. 2017. "An Apparatus for the Investigation of Turbulence on the Erosion–Corrosion of Piping Materials." Corrosion 2017, New Orleans, LA, 26–30 Mar 2017.
- Det Norske Veritas. "Multiphase Flow Laboratory at DNV–GL." Accessed 05 Jan 2018.
<https://www.dnvgl.com/news/taking-the-multiphase-flow-laboratory-in-groningen-to-maximum-capacity-6374>.
- Eisenberg, D., and W. Kauzmann. 1969. *The Structure and Properties of Water*. New York: Oxford University Press.
- Greenblatt, B. M. 2017. "VTHTCL Flow Rate versus Motor Frequency Calibration." Homework assignment for Undergraduate Research, Materials Science and Engineering Department. Virginia Tech, Blacksburg, VA.

- H. H. Vanhout, III. 2017. "Heat Flow from the Virginia Tech High Turbulence Corrosion Loop." Homework assignment for Undergraduate Research, Materials Science and Engineering Department. Virginia Tech, Blacksburg, VA.
- Holman, J. J. 2002. *Heat Transfer*. 9th ed. New York: McGraw Hill.
- Idaho National Laboratory. "Multi-Purpose Thermal Hydraulic Test Facility at Idaho National Laboratory." Accessed 05 Jan 2018.
<https://inldigitallibrary.inl.gov/sites/sti/sti/6340998.pdf>.
- Institute for Energy Technology Norway. "Materials and Corrosion Technology Department." Accessed 5 Jan 2018. <https://www.ife.no/en/ife/laboratories/hastelloy/hastelloy-loops>.
- ISO 2007. Standard ISO209:207, in *Aluminum and aluminum alloys – Chemical composition*. Geneva, Switzerland: International Organization for Standardization. (Note: Available from ANSI.)
- Jones, D. A. 1992. *Principles and Prevention of Corrosion*. New York: Macmillan Publishing.
- Jorgensen, F. E. 2002. Technical Report *How to Measure Turbulence with Hot-Wire Anemometers: A Practical Guide*. Skovlunde, DK: Dantec Dynamics.
<https://www.dantecdynamics.com/docs/support-and-download/research-and-education/practicalguide.pdf>, accessed 18-Feb-2018.
- Knight, M. "Chemical Resistance and Chemical Applications for CPVC Pipe and Fittings." Schaumburg, IL: Chemical Processing Accessed 22 May 2017.
http://www.chemicalprocessing.com/assets/wp_downloads/pdf/ChemicalResistanceWhitePaperFINAL.pdf.
- Lawe, J. Personal communication with R. W. Hendricks, 27 Mar 2017.
- Lones, J. R., T. C. Strickland, H. A. Van Hout III, and J. P. Zilke. 2017. "Corrosion of 2024-T-3 Aluminum in Highly Turbulent Sea Water." Homework assignment for Senior Design, Materials Science and Engineering Department. Virginia Tech, Blacksburg, VA.

- Massachusetts Institute of Technology. "BWR Water Loop in the H. H. Uhlig Corrosion Laboratory at MIT." Accessed 05 Jan 2018.
<http://web.mit.edu/uhliglab/capabilities.shtml>.
- Meritt, R. J., and J. A. Schetz. 2016. "Skin Friction Sensor Development, Validation, and Application for High-Speed, High-Enthalpy Flow Conditions." *Journal of Propulsion and Power* 32 (4):821–833. doi: <https://doi.org/10.2514/1.B35917>.
- Metal Samples. 2018a. Technical Report *Introduction to ER Monitoring*. Munford, AL: Metal Samples. <http://www.alspi.com/erintro.htm>, accessed 07-Jan-2018.
- Metal Samples. 2018b. Technical Report *Electrodes*. Munford, AL: Metal Samples. <http://www.alspi.com/electrodes.htm>, accessed 07-Jan-2018.
- Metal Samples. 2018c. Technical Report *Linear Polarization Resistance (LPR) Monitoring*. Munford, AL: Metal Samples. <http://www.alspi.com/lprintro.htm>, accessed 07-Jan-2018.
- Miller, I., and J. E. Freund. 1977. *Probability and Statistics for Engineers (2E)*. Englewood Cliffs, NJ: Prentice Hall.
- Munson, B. R., T. H. Okiishi, W. W. Huebsch, and A. P. Rothmayer. 2013. *Fundamentals of Fluid Mechanics*. 7th ed. Hoboken, NJ: John Wiley and Sons.
- MyDatabook.org. 2018. "Flow Coefficient, Opening and Closure Curves of Full Bore Ball Valves." Accessed 13-Feb-2018. <http://www.mydatabook.org/fluid-mechanics/flow-coefficient-opening-and-closure-curves-of-full-bore-ball-valves/>.
- Oak Ridge National Laboratory. "Corrosion Science and Technology at Oak Ridge National Laboratory." Accessed 05 Jan 2018. <https://www.ornl.gov/division/mstd/corrosion-science-and-technology>.
- Ohio University. "Institute for Corrosion and Multiphase Technology at Ohio University." Accessed 05 Jan, 2018. <https://www.ohio.edu/engineering/corrosion/facilities-equipment/facilities.cfm>.
- Omega Engineering. 2009. Technical Report M-4517/0109: *FTB-1400 Series Economical Liquid Turbine Flow Meters Specification Sheet*. Stamford, CT: Omega Engineering. http://www.omega.com/green/pdf/FTB1400_SERIES.pdf, accessed 3 Jun 2017.

- Panton, R. L. 2013. *Incompressible Flow*. 4th ed. Hoboken, NJ: John Wiley and Sons.
- Ponthiaux, P., F. Wenger, and J.-P. Celius. 2012. "Material Behavior Under Combined Conditions of Corrosion and Mechanical Loading." In *Corrosion Resistance*, edited by Dr. Shih. Rijeka, Croatia: InTech Europe.
- SAE. 2017. *Unified Numbering System for Metals and Alloys (UNS)*. 13th ed. Warrendale, PA: SAE International.
- Schetz, J. A. 2010. "Direct measurement of Skin Friction in Complex Flows." *AIAA Paper* 2010-44.
- Spears. undated. Technical Report *Spears Engineering Sourcebook*. Sylmar, CA: Spears Manufacturing http://63.156.201.111/SMC/SELECTIOND_SLECTIOND.htm-SELEFVFL, accessed 5-Feb-2018.
- Todoroff, P. K. 2018. "Investigation of Turbulence on the Passivation Film Growth and Associated Durability for Aluminum Alloys in Simulated Seawater Naval Heat Exchanger." MSc, Materials Science and Engineering, Virginia Tech.
- Tuthill, A. 1987. "Guidelines for the use of copper alloys in seawater." *Materials Performance* 26 (9):12-22.
- Universiti Teknologi PETRONAS (UTP). "Flow Assurance Test Loop." Accessed 05 Jan 2018. <http://www.synergykl.com.my/innovation.html>.
- University of Michigan. "High Temperature Corrosion Laboratory at the University of Michigan." Accessed 05 Jan 2018. <http://www.mse.engin.umich.edu/people/gsw/facilities/high-temperature-corrosion-laboratory-htcl>.
- University of Tulsa. "Tulsa University Fluid Flow Projects." Accessed 05 Jan, 2018. <http://www.tuffp.utulsa.edu/facilities.html>.
- Williams, G. S., and A. Hazen. 1914. *Hydraulic tables: the elements of gagings and the friction of water flowing in pipes, aqueducts, sewers, etc., as determined by the Hazen and Williams formula and the flow of water over sharp-edged and irregular weirs, and the quantity discharged as determined by Bazin's formula and*

experimental investigations upon large models. . 2nd revised and enlarged ed. New York, NY: John Wiley and Sons.